

# Rapid wavefront shaping using an optical gradient acquisition

SAGI MONIN,<sup>1</sup> MARINA ALTERMAN,<sup>1</sup> AND ANAT LEVIN<sup>1,\*</sup>

<sup>1</sup>*Department of Electrical and Computer Engineering, Technion, Israel*

\**anat.levin.g@gmail.com*

## 1. Abstract

Wavefront shaping systems enable deep imaging inside scattering tissue by correcting aberrations caused by tissue inhomogeneity. However, estimating optimal modulations remains challenging as such modulations depend on the unknown tissue structure. Most current techniques employ slow coordinate descent algorithms, which sequentially scan all modulation elements and query their values independently. Thus, their complexity scales prohibitively with the number of modulation parameters. We present a rapid wavefront shaping method that transitions from coordinate to gradient descent optimization, simultaneously updating all modulation parameters. Our approach employs a non-invasive, guide-star-free score function to quantify modulation effectiveness. We derive an analytical framework expressing the score's gradient with respect to all parameters. Although this gradient depends on the unknown tissue structure, we demonstrate how it can be inferred from optical measurements. This method enables rapid computation of high-resolution wavefront corrections, with complexity independent of the number of modulation parameters. High resolution modulations enable superior correction in thicker tissue samples. We demonstrate our framework's efficacy in correcting aberrations in a coherent confocal microscope.

## 2. Introduction

Optical imaging of tissue is challenging because cells and other tissue components scatter light. As a result, as light propagates deeper into tissue, it becomes heavily aberrated, making it challenging to resolve clear images of deeper structures. Over the decades, several techniques, such as confocal microscopy [1] and optical coherence tomography (OCT) [2], have been developed to achieve deeper imaging by filtering out scattered photons and isolating ballistic photons to form an image. Despite this progress, these techniques are inherently limited to thin layers as the number of ballistic photons decays rapidly within scattering materials. To overcome this challenge, wavefront shaping was introduced. Instead of filtering out the scattered photons, wavefront shaping aims to measure the scattered light and invert the process. Such corrections follow two major approaches: digital and optical.

Digital aberration correction methods attempt to illuminate the tissue using a set of wavefronts and measure the scattered light. This data is fitted with a parametric model to estimate the aberration and reconstruct the hidden target [3–21]. This approach has led to impressive results, but it is ultimately limited by signal-to-noise ratios (SNR). Even with advanced gating strategies, light scattered by deeper tissue components is weak and can be lost in measurement noise.

An alternative class of techniques uses optical wavefront-shaping [22–26]. Such techniques use spatial light modulators (SLMs) to control the incoming and/or outgoing paths of the optical system. These SLMs reshape the incoming and/or outgoing wavefront in a way that is the inverse of the aberration it undergoes inside the tissue. This allows an incoming wavefront to focus to a diffraction-limited spot, and the light emitted from a single point within the tissue can be focused onto a single detector element. Unlike digital aberration corrections, the significant advantage of optical wavefront shaping is that the correction is physical; hence, all light photons emerging from a single target point can be brought into a single sensor point and measured with a significantly higher SNR.

Wavefront shaping ideas have found applications in a wide range of imaging modalities, including sound [24, 27] and light, coherent imaging and OCT [28], and incoherent fluorescence imaging using single-photon [29–32] and multi-photon [22, 33] excitation. This work showcases a simple aberration correction in a coherent, reflection mode confocal microscope. However, our framework also applies to other popular imaging schemes such as OCT and fluorescent microscopy.

The practical application of wavefront shaping is hindered by the complexity of determining the desired modulation correction. This wavefront correction differs between different tissue samples, and vary even within different regions of the same tissue sample. Earlier proof-of-concept demonstrations employed a validation camera behind the tissue to provide feedback for the algorithm [34–39]. Other approaches utilize a guide star [24, 28, 33, 40–47], where scattering originates from a strong single point source within the tissue, allowing a wavefront sensor [42, 47] to directly measure the scattered wavefront.

In the absence of such a guide-star, determining a wavefront shaping correction is a significantly more challenging task. Most approaches define a score function to evaluate the quality of the modulation based on the captured signal, and then optimize the SLM parameters to maximize this score. A core challenge for such optimization algorithms lies in the unknown structure of the tissue. This structure can only be probed by projecting multiple modulation patterns and imaging their scattered output. Thus, most wavefront shaping optimization schemes employ coordinate-descent (CD) approaches, where a single parameter of the modulation is varied at a time. Each optimization step involves selecting a new value for one parameter to improve the modulation score. These algorithms iterate sequentially through all degrees of freedom [29, 31, 33–35, 39, 48]. The main drawback of coordinate descent schemes is their time complexity, which scales with the number of free parameters in the modulation. For thick tissue, the modulation should ideally use all pixels on the SLM, usually in the megabyte range.

In this research, we derive a fast approach for estimating a wavefront-shaping correction in a non-invasive, guide-star free setting. *Our algorithm is capable of simultaneously updating all SLM parameters from the information in one measurement*, and explicitly optimize a desired score function. To this end, we start by analytically differentiating the wavefront-shaping score. Although the gradient depends on the unknown tissue structure, we show we can use optical computing to measure it. By simply capturing the back scattered field, the gradient can be evaluate in closed-form. The dimensionality of the gradient vector is equivalent to the number of SLM parameters. With this gradient at hand, we can simultaneously update all SLM parameters, and we can transition from slow coordinate descent to fast gradient descent optimization.

Our gradient descent scheme is significantly faster than existing coordinate descent schemes and can also recover better modulations. Coordinate descent methods typically restrict the number of SLM modes they optimize due to computational complexity and since the measurement of high-frequency modes is noise sensitive. However, in thick tissue where the scattering is wide, the optimal modulation requires a large number of degrees of freedom. In contrast, our approach can optimize a large number of modes without an increase in computational complexity. We show that this higher number of modes allows us to find significantly better modulations.

### 3. Results

#### 3.1. Background

**Imaging setup:** In Fig. 1, we visualize a wavefront-shaping imaging setup. A laser beam illuminates a tissue sample via a microscope objective. A phase SLM in the illumination arm modulates the illumination pattern. Our objective is to image a target within the tissue layer. Coherent light back-scattered from the target is collected by the same objective lens and reflected by a beam-splitter. A second phase SLM in the imaging arm modulates the returning wavefront.

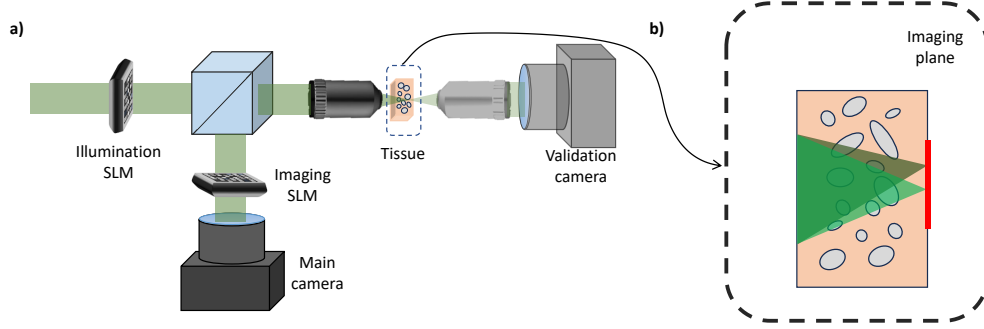


Fig. 1. **System Schematic:**(a) Schematic diagram of our system consisting of two SLMs. The first SLM modulates the illuminating laser light, while the second SLM modulates the reflected light. A validation camera provides reference images and confirms focusing on the desired target. (b) Our algorithm optimizes SLM phase to focus light on multiple adjacent points, by applying simple tilt-shift to the same modulation.

Lastly, the modulated light is measured by the front main camera. The two SLMs in our setup are conjugate to each other. Our setup incorporates a validation camera positioned behind the tissue sample. This camera serves to evaluate focusing quality and capture an undistorted reference image of the target. While earlier research demonstrations of wavefront-shaping utilized this camera to provide feedback to the algorithm, here we develop a non-invasive technique relying solely on feedback by the main (front) camera. It is crucial to note that the validation camera serves only for reference and *does not* provide any input to our algorithm.

To maximize the correctable area with a single modulation, the SLM should ideally be placed conjugate to the aberration [49], namely to a plane in the middle of the tissue. For simplicity, in our experimental setup, the SLMs are placed in the Fourier plane. To correct aberrations across a wide field of view with a single modulation pattern, we apply a tilt and shift operation to the Fourier pattern [50, 51]. The two SLMs in our setup are placed such that they are conjugate to each other.

**Image formation model:** We start by presenting a generalized image formation model for a dual SLM system, comprising an illumination SLM and an imaging SLM. Based on this model we derive the specific model of our imaging system.

We denote the reflection matrix of the tissue as  $\mathcal{R}$ . This matrix describes propagation of light from the illumination SLM plane through the tissue and optics, and back to the imaging SLM. Thus, for every wavefront  $\mathbf{u}^i$  placed on the illumination SLM, the resulting wavefront reaching the imaging SLM is modeled as a linear transformation by the reflection matrix:

$$\mathcal{R}\mathbf{u}^i. \quad (1)$$

Applying a modulation  $\mathbf{u}^o$  to the imaging SLM, the wavefront reaching the camera is:

$$\mathcal{Z} \left( \mathbf{u}^o \odot (\mathcal{R}\mathbf{u}^i) \right), \quad (2)$$

where  $\mathcal{Z}$  denotes a linear mapping between the imaging SLM and the camera sensor that can be calibrated and described by a 2D matrix as it is independent of the tissue sample.  $\odot$  represents element-wise multiplication between two vectors.

Our objective is to use a single SLM modulation to image a small area inside the volume rather than a single point. For that we denote the modulation parameters (the phase values of the SLM)

as  $\rho^i, \rho^o$ . To direct this modulation to adjacent points within the scattering tissue, we apply tilt and shift to the SLM modulation [50, 51]. We represent the tilt-shifted modulation directed towards volume point  $\ell$  as  $\mathbf{u}^\ell(\rho^i)$ . This notation implies that  $\rho^i$  are the parameters we can adjust, from which we derive multiple modulations  $\mathbf{u}^\ell(\rho^i)$  by applying fixed tilt-shift operations toward different points  $\ell$ . Similarly,  $\mathbf{u}^\ell(\rho^o)$  denotes a tilt-shifted modulation on the imaging SLM. With this tilt-shift, light emerging from different points  $\ell$  in the volume arrives at the same position on the sensor:

$$\mathcal{Z} \left( \mathbf{u}^\ell(\rho^o) \odot (\mathcal{R}\mathbf{u}^\ell(\rho^i)) \right). \quad (3)$$

The intensity at pixel  $x$  of the camera is:

$$I(x) = |\zeta_x \odot \mathbf{u}^\ell(\rho^o))^T \mathcal{R}\mathbf{u}^\ell(\rho^i)|^2, \quad (4)$$

where  $\zeta_x$  is row of the matrix  $\mathcal{Z}$  mapping the output of the SLM to a pixel  $x$  on the camera.

In our system,  $\mathcal{R}$  models the coherent propagation of a monochromatic laser beam. However, this formulation can be generalized to describe other forms of propagation, such as path-length resolved reflection matrix describing the measurements of an OCT system. Also,  $\mathcal{Z}$  can represent various mappings between the imaging SLM plane to the camera sensor plane, depending on an optical setup of choice. In our system, we place the SLM in the Fourier plane; hence,  $\mathcal{Z}$  is a Fourier transform.

**Score function:** We aim to develop an optimization framework that identifies the optimal wavefront modulation for focusing light at a designated plane within scattering tissue. To achieve this, we start by defining a score  $\mathcal{S}(\rho)$  which can quantify a good modulation. We will then attempt to maximize this score to obtain a good modulation:

$$\hat{\rho} = \arg \max_{\rho} \mathcal{S}(\rho). \quad (5)$$

To identify a good modulation in a non-invasive, guide-star free setting, we build upon the work of [31] and recent digital correction approaches [9, 10, 14]. We measure the confocal energy of the corrected area. We apply the same modulation  $\rho^i = \rho^o$  on both illumination and imaging SLMs and denote it by a single parameter vector  $\rho$ . We direct and collect light from a point  $\ell$  and measure the intensity at the central sensor pixel. In our system, the mapping between the SLM and the camera is a Fourier transform. Consequently, the central pixel corresponds to the DC component of the Fourier transform (i.e.  $\zeta_x$  is a uniform vector). Following (4), we can express the measured confocal energy as:

$$I(0) = |\mathbf{u}^\ell(\rho)^T \mathcal{R}\mathbf{u}^\ell(\rho)|^2. \quad (6)$$

We sum the confocal intensity over an area and measure the total intensity we can collect by a confocal scanning of the modulation, tilted toward different points  $\ell$  in an area of interest  $\mathcal{A}$ :

$$\mathcal{S}(\rho) \equiv \sum_{\ell \in \mathcal{A}} |\mathbf{u}^\ell(\rho)^T \mathcal{R}\mathbf{u}^\ell(\rho)|^2. \quad (7)$$

To better illustrate this score, Fig. 2 visualizes the incident and reflected wavefronts, both with and without modulation, for various points within the target area. Initially, without modulation, these wavefronts exhibit minimal correlation. However, once we find a focusing modulation the incoming and outgoing wavefronts demonstrate high correlation. Additionally, we observe a strong memory effect correlation among wavefronts returning from different points.

We note that in [31] incoherent fluorescence signal was collected and the confocal energy was measured at a single pixel, without attempting to average over an area. Since we use coherent light, we notice that if we only direct light to a single spot, a high confocal score at the sensor



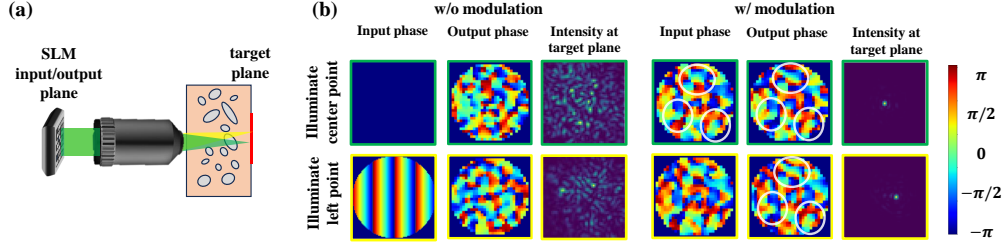


Fig. 2. **Tilt-shift and time reversal effects:** (a) We show a simplified schematic of our system with two input wavefronts, green focusing into the center of the imaging plane and yellow focusing to a neighboring point to the left. (b) Simulation results showing the incoming phase on the SLM, the conjugate of the output phase after tissue reflection (when reaching the SLM plane), and the intensity at the target plane. With light modulation, strong correlations are observed between the incoming SLM phase and the output phase, as well as between output phases for different points (white circles indicate areas of strong correlation). Without aberration correction, correlation decreases rapidly.

plane does not guarantee that the light has focused into a single spot inside the tissue, due to various interference effects. To address this, we propose averaging the confocal score over a *small* area  $\mathcal{A}$ , which mitigates these interference effects. This approach aligns with recent coherent digital correction algorithms [9, 10, 14], that optimize over finite isoplanatic patches to maximize the diagonal elements of the reflection matrix which is equivalent to the confocal area score. The supplementary file provides a short derivation justifying the score using local memory effect correlations. We investigate the impact of the target area size on focusing performance in our experimental section, and show that in practice one modulation can only be used over very small area, due to the limited extent of memory effect correlations.

### 3.2. Optical gradient acquisition

The main challenge in utilizing the score defined in Eq. (7) lies in its dependence on the tissue's reflection matrix, which is inherently linked to the unknown tissue structure. Since the tissue is treated as a black box, most previous approaches have employed coordinate descent optimization strategies [29, 31, 33–35, 48]. In each iteration, only one parameter is varied (often in a Hadamard basis) and adjusted to improve the measured score. For invasive setups, the score is simply the intensity measured by a validation camera at a point behind the tissue. Given that modern SLMs are in mega-pixel resolution, sequentially scanning each free parameter is an extremely time-consuming process. Consequently, researchers frequently reduce the SLM resolution and correct a significantly smaller number of modes. Below we derive a scheme for simultaneously measuring the gradient with respect to all SLM parameters. This approach enables us to transition from coordinate descent schemes to a gradient descent scheme, that *updates all SLM parameters in each iteration*.

We start by applying the chain rule and differentiate Eq. (7) with respect to the SLM parameters  $\rho$ :

$$\frac{\partial S(\rho)}{\partial \rho} = 2 \sum_{\ell} \underbrace{\left( \mathbf{u}^{\ell}(\rho)^T \mathcal{R} \mathbf{u}^{\ell}(\rho) \right)^*}_{(1)} \cdot \underbrace{\left( \mathcal{R} \mathbf{u}^{\ell}(\rho) + \left( \mathbf{u}^{\ell}(\rho)^T \mathcal{R} \right)^T \right)}_{(2)} \odot \underbrace{\frac{\partial \mathbf{u}^{\ell}(\rho)}{\partial \rho}}_{(3)}. \quad (8)$$

This gradient is a product of three terms. The first (1) is a complex scalar. The second (2) is a complex vector whose dimensionality is equivalent to that of the modulation. The third term (3),

which differentiates the wavefront with respect to the parameters  $\rho$ , can be computed explicitly. As we explain in the supplementary, since  $\mathbf{u}^\ell(\rho)$  simply shift and multiplies the elements of  $\rho$  by complex tilt scalars, the derivative with respect to  $\rho$  is also a simple tilt-shift of the derivative with respect to  $\mathbf{u}^\ell(\rho)$ .

The challenge with the first two terms is that they involve the unknown reflection matrix  $\mathcal{R}$ . Nevertheless, we can leverage the optics to measure the gradient in Eq. (8) for any candidate modulation  $\rho$  of interest. We observe that the complex field  $\mathcal{R}\mathbf{u}^\ell(\rho)$  is essentially equivalent to applying a modulation at the illumination arm only, and capturing a non-modulated speckle field. The complex field can be captured using a phase retrieval algorithm or with an interferometric imaging system, as detailed in supplementary material. With this measurement, we can numerically compute the remaining terms of Eq. (8). For example, following the reciprocity principle,  $\mathcal{R}$  is a symmetric matrix and  $(\mathbf{u}^\ell(\rho)^T \mathcal{R})^T$  is equal to  $\mathcal{R}\mathbf{u}^\ell(\rho)$ . Similarly, the term (1) in Eq. (8) can be computed by multiplying  $\mathcal{R}\mathbf{u}^\ell(\rho)$  with the known vector  $\mathbf{u}^\ell(\rho)$ .

By measuring the gradient of the modulation score *we can simultaneously update all entries of the SLM*. This offers a substantial acceleration compared to previous approaches, which iterate through the entries and update only one degree of freedom at a time.

In our current implementation we measured the fields  $\mathcal{R}\mathbf{u}^\ell(\rho)$  using a phase diversity scheme. This involved applying five defocus wavefronts to the imaging SLM [52, 53], capturing five speckle intensity images, and solving an optimization problem for recovering the phase [54]. We measure each of the  $\ell$  points and sum them. In the supplementary material, we show that the gradient can in fact be imaged directly using a point-diffraction interferometry scheme [55, 56], bypassing the optimization. Moreover, the summation across all points  $\ell$  can be computed within a single exposure, hence the entire gradient can be imaged with as little as 3 shots.

In the supplementary file we also explain that the gradient descent approach derived above resembles fast wavefront shaping algorithms based on time reversal and the power algorithm [27, 30, 57–60]. In fact, it is equivalent to a power iteration of the reflection matrix, if one aims to maximize confocal intensity at a single spot rather than an area. However as we show below a single spot score does not result in good modulations. While power iterations are tied to an eigenvector calculation and may not be adjusted easily to optimize other things, defining a general score function and its gradient provides a more principled way to impose all sort of desired properties on the solution.

The optical calculation of the gradient here also resembles the derivation in [61]. However, their system uses transmission mode imaging and thus requires two SLMs on two sides of the scattering medium.

### 3.3. Experimental results

In our experiments we used two types of targets. The first consisted of high-reflectance chrome-coated masks (Nanofilm), patterned using an in-house lithography process to create structures with a resolution of  $2\mu\text{m}$ . We placed these behind scattering layers composed of chicken breast tissue with thickness of  $130\mu\text{m} - 240\mu\text{m}$  or with a number of layers of parafilm [62]. The second target includes polystyrene beads dispersed in agarose gel.

**Convergence:** In Fig. 3 we cover the chrome mask with  $180\mu\text{m}$  thick chicken breast, and demonstrate the algorithm’s efficiency, converging to the desired spot in as few as ten iterations, compared to thousands required by previous coordinate descent algorithms. We show an image of one of the points  $\ell$  in the optimized area  $\mathcal{A}$ , with no modulation and when the optimized modulation is placed on both SLMs. Without modulation we see a noisy speckle image but with the modulation we see a sharp spot whose intensity is about 20× higher. We also image the chrome mask directly using the validation camera. Without modulation we see a wide speckle pattern, but with the optimized modulation on the illumination arm all light propagates through the scattering layer and is focused into a single point on the chrome mask. These validation

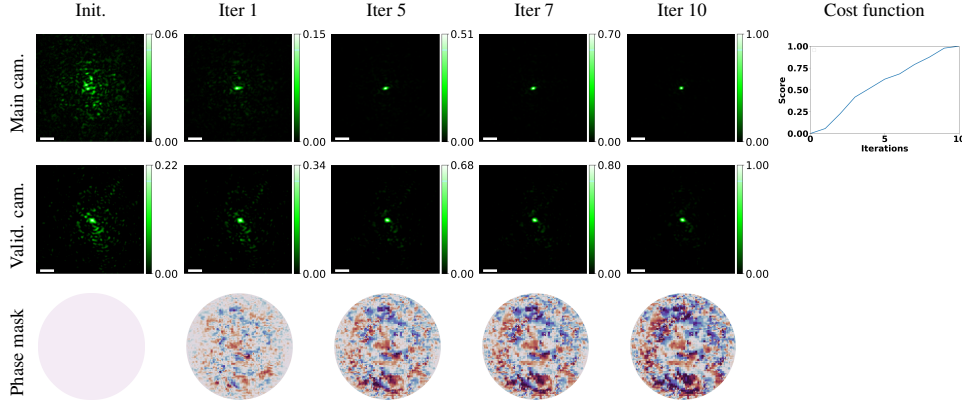


**Fig. 3. Algorithm convergence:** We used our algorithm to image a glass mask partially covered with chrome, placed behind a  $180\mu\text{m}$  thick chicken breast tissue as the scattering material. We show captured images on both the main and validation cameras before the algorithm is applied and at the end of each iteration. The first row demonstrates the algorithm's convergence over iterations on the main camera for one of the scanned points. The second row displays the convergence on the validation camera, demonstrating our ability to also focus light on the target plane. The final row depicts the evolution of the phase mask presented on both SLMs. The last column illustrates the improvement of the cost function across iterations. Scale bar is  $4\mu\text{m}$ .

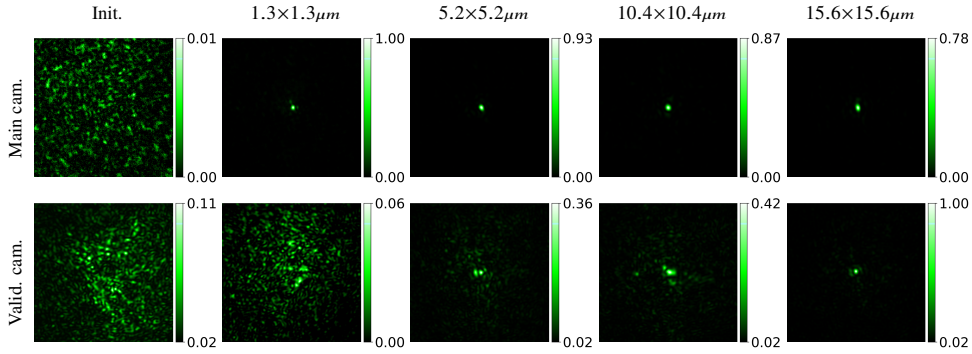


**Fig. 4. Effect of target area size:** We evaluate how focusing quality depends on the size of the target area  $\mathcal{A}$  over which the confocal score is computed. The experiment used a chrome-covered glass mask overlaid with  $240\mu\text{m}$  thick chicken breast tissue. Our results show that for single-spot illumination (second column) the algorithm successfully achieved a sharp focused spot on the main camera without actually focusing light to a spot inside the tissue, as evident by the image from the validation camera. As we expanded the size of the focus area, the algorithm demonstrated progressively improved ability to focus light inside the tissue and the validation camera images are sharper. At the same time increasing the scanned area reduces the intensity of the focused spot on the main camera because a single modulation cannot correct very large areas.

images ensure that the point we see in the main camera indeed corresponds to a point on the

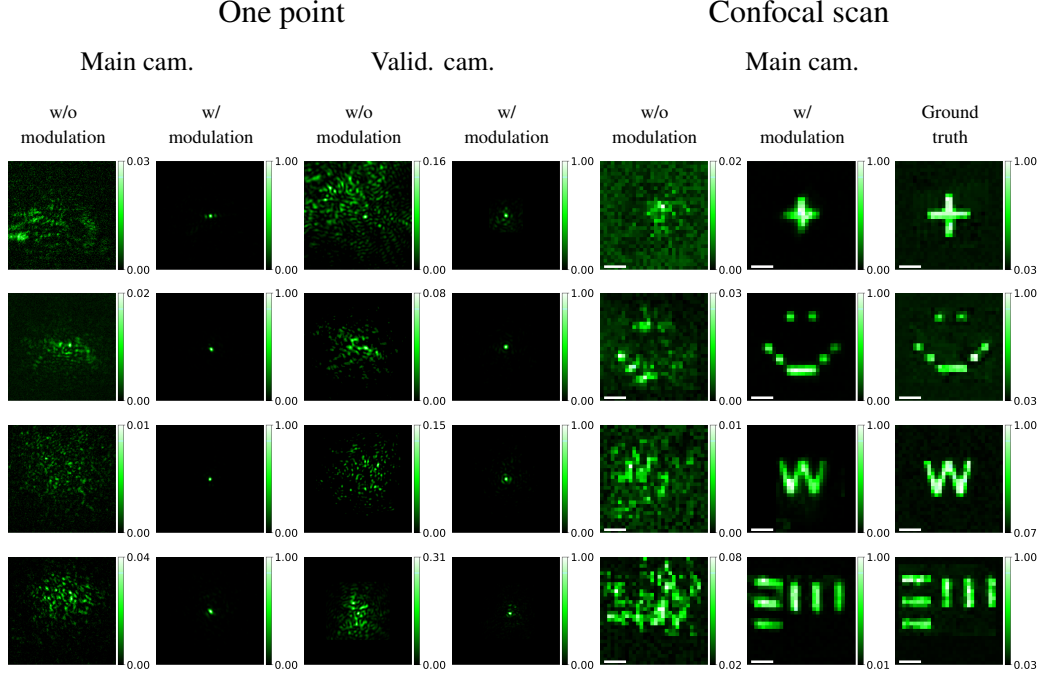


Fig. 5. **Confocal imaging:** of patterns printed on chrome mask, through a scattering layer. Our algorithm successfully focuses light on the desired plane. Each row shows a different target. Columns 1-2: Main camera images of a single focal spot before and after optimization. Columns 3-4: Corresponding validation camera images. Columns 5-7: Confocal scanning results: Without aberration correction, with aberration correction, and reference scan of the target before applying scattering material, respectively. In the first three targets (top rows) the scattering material is chicken breast of thickness of  $130\mu\text{m}$ ,  $150\mu\text{m}$  and  $200\mu\text{m}$ , respectively. In the fourth target the scattering material is two layers of parafilm. Scale bar on confocal images is  $4\mu\text{m}$ .

mask, and we are not achieving a point on the main camera by complicated interference effects inside the tissue. At the lower row we show the progress of the phase mask during the iterations.

**Impact of scanned area:** In Fig. 4, we evaluate the effect of the area  $\mathcal{A}$  over which the score is optimized. If this area is small we observe a sharp spot at the main camera but the light did not actually focus into a spot inside the tissue as we do not observe a spot at the validation camera. This indicates that the spot at the main camera results from interference of coherent light within the tissue. This issue does not occur with fluorescent wavefront shaping [31] since the incoherent emissions from nearby fluorescent points do not interfere. As we increase the size of the scanned area, requiring the same modulation to explain multiple points, such interference effects disappear, and we achieve a point in both cameras. However, as we increase the target area the intensity of the focused spot at the main camera decays because the correction required by nearby points vary spatially and one modulation cannot explain a wide area. This is due to the fact that memory effect correlation does not hold for very large ranges. Note that our score function recovers modulations using a non-invasive, guide-star free feedback.

**Confocal imaging:** In Fig. 5, we present imaging results for a few patterns printed on the chrome mask. We display images of a single point in the area through both the main and validation cameras. We also show a confocal scan of the entire area. Without modulation, this looks like a

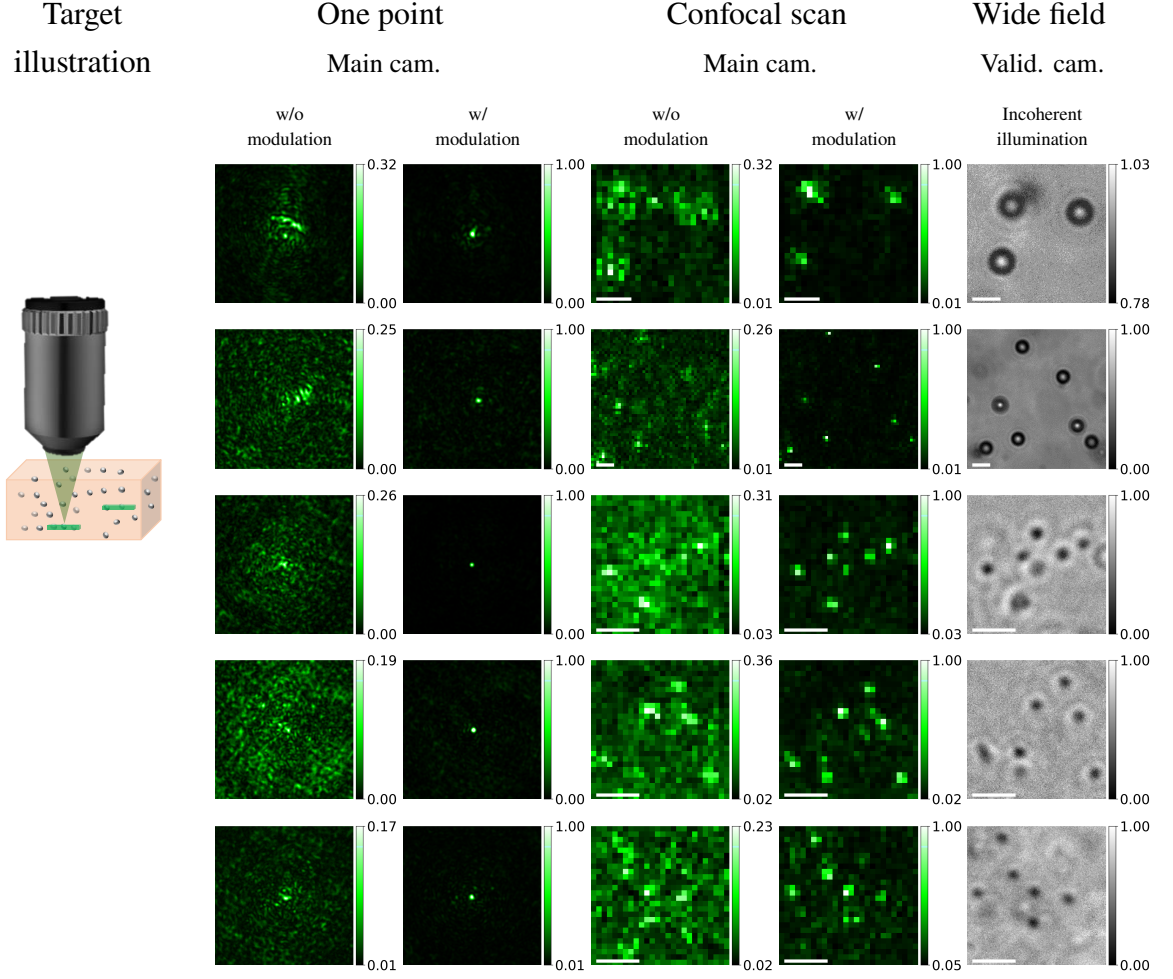


Fig. 6. **Confocal scan of beads:** Our algorithm used to image a scattering dispersion of polystyrene beads in agarose gel. The first column depicts a schematic view of the target, where we image small regions in different spatial areas and varying depth of the gel. The green bars inside the target depict the different areas which were imaged. Columns 2-3: Main camera images of a single focal spot before and after correction. Columns 4-5: Confocal scanning results: with and without aberration correction. Column 6: A reference image of the target captured from the validation camera behind the target, under wide-field incoherent illumination. Rows 1-2 use  $3\mu\text{m}$  diameter beads and rows 3-5 use  $0.5\mu\text{m}$  diameter beads. Scale bar on confocal images is  $4\mu\text{m}$ . Note that an ideal aberration free image of beads in a reflection mode confocal microscope is a diffraction limited spot [63], even if the beads are larger than the diffraction limit since they act as a mini-lens focusing light.

speckle pattern; however, with the modulation, the confocal scan reveals the shape of patterns printed on the chrome mask. Note how the modulation increases light by a factor 12 – 100×.

**Bead targets:** We demonstrate that our algorithm can also image translucent targets with small variations in refractive indices. To do this we disperse polystyrene beads in agarose gel. Polystyrene and agarose have refractive indices of approximately 1.598 and 1.334 under our  $532\text{nm}$

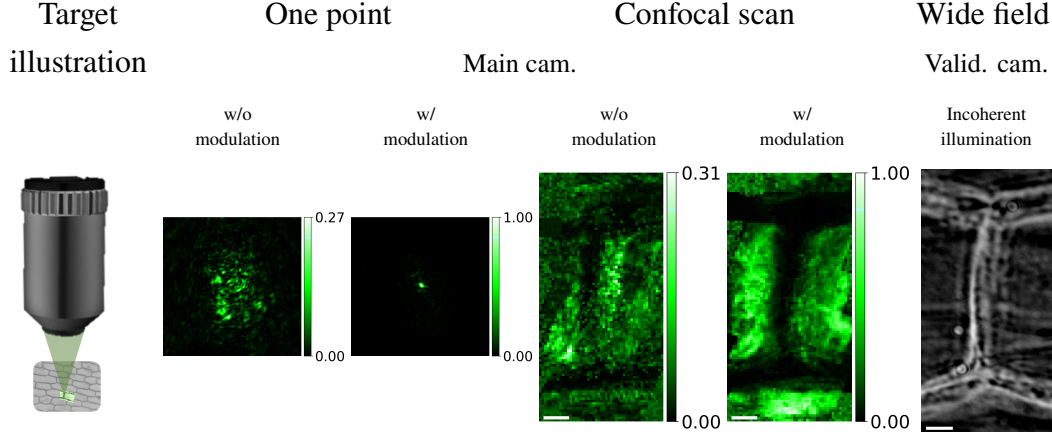


Fig. 7. **Confocal scan of onion cells:** Our algorithm used to image onion cells inside a  $130\mu\text{m}$  thick onion slice. First column: an illustration of the target. Columns 2-3: Main camera images of a single focal spot before and after correction. Columns 4-5: Confocal scanning results: with and without aberration correction. Column 6: A reference image of the target captured from a validation camera behind the target, under wide-field incoherent illumination. Scale bar is  $5\mu\text{m}$ .

illumination, and thus are within the range found practically in tissue. We create two different targets, with bead diameters  $0.5\mu\text{m}$  and  $3\mu\text{m}$ . The slab thickness is  $1.3\text{mm}$ . The left part of Fig. 6 illustrate the schematic of this target, where we used our algorithm to focus inside this volume, and image planar sub-regions at multiple depths. The optical depth (OD) is 3, where OD was estimated by measuring the attenuation of ballistic light in the validation camera. In Fig. 6 visualize our confocal scanning results. While a standard confocal scan of such beads is very noisy, with our estimated modulation we can largely increase its contrast and achieve a clear image of spots corresponding to the beads position. To obtain a reference image of the bead positions, we image beads at the further depth of the slab closer to the validation camera, so we are able to image a clear reference from the validation camera. For this reference image, we used a wide-field incoherent illumination.

**Onion slice:** Utilizing our algorithm, in Fig. 7 we successfully imaged onion cells through a  $130\mu\text{m}$  thick slice of highly scattering onion [64]. Specifically, we visualized the intercellular boundary between two neighboring cells. In the supplementary material we show a larger field-of-view of the onion under incoherent illumination. In addition, we show a confocal scan of an onion cell at a shallower layer, where scattering does not limit image quality. The aberration-corrected result in Fig. 7 matches this unaberrated structure.

Some of our results image areas bigger than the range of memory effect correlation and cannot be considered as a single iso-planatic patch. We imaged such targets by applying multiple local corrections and stitching a few patches together. In the supplementary material Figs. S6 and S7 we show the different iso-planatic patches.

In the following paragraphs we use again the chrome mask target to evaluate various components of our algorithm.

**Impact of resolution:** Our approach is significantly faster than coordinate descent schemes which scan each SLM mode independently. In practice, to reduce scan time coordinate descent schemes optimize for a relatively small number of modes. For thick tissue, where the scattering is wide we actually need a large number of modes to obtain a good correction. In Fig. 8, we

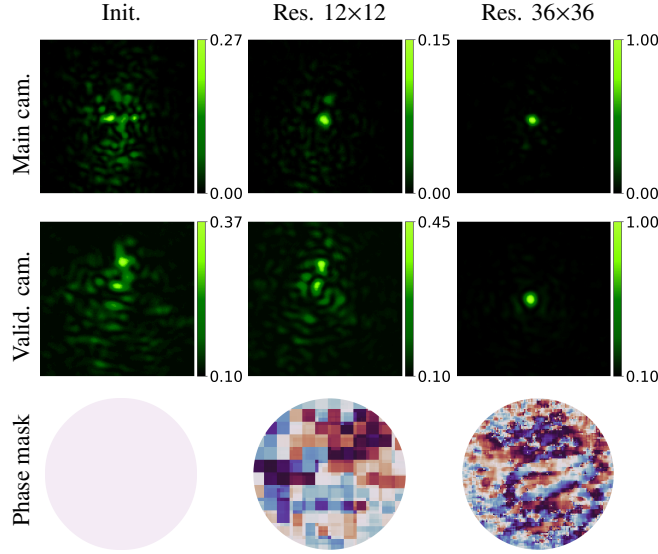


Fig. 8. **Impact of phase mask resolution:** We evaluate the effectiveness of gradient descent (GD) solutions using phase masks of varying resolutions. We place the chrome mask behind two layers of parafilm, creating a significant aberration. Results demonstrate that higher-resolution phase masks yield superior solutions, enabling convergence in both the main and validation cameras.

demonstrate the impact of resolution on the quality of the correction. As shown, a modulation with more degrees of freedom allows us to focus more energy into a single spot.

**Comparison with coordinate descent optimization:** Next we explicitly compare our gradient descent scheme with a coordinate descent approach. Following [31,36], we express the modulation as  $\rho = \sum \phi_k H_k$  where  $H_k$  are elements in an Hadamard basis. We scan the basis elements, adjusting the phase of one basis element at a time. We argue that the resolution of coordinate descent schemes is not only limited by acquisition time, but also by SNR. For high frequency modes, varying  $\phi_k$  results in a very small change to the score, potentially lower than the noise level. In Fig. 9 we show that the coordinate descent score cannot improve beyond a certain point. To illustrate that noise is the limiting factor, we run another coordinate descent scheme, but this time we averaged multiple shots for each basis element to reduce noise. This oversampling approach allowed us to update the high frequency modes, leading to much better results. However, the oversampling is also  $5\times$  slower than the standard coordinate descent scheme and  $125\times$  slower than our gradient descent scheme. The modulation computed in Fig. 9 is a low-resolution one. For higher resolution modulations the time difference between coordinate descent and gradient descent approaches would be even larger.

#### 4. Discussion

The challenge in computing a wavefront shaping modulation lies in its dependence on the unknown tissue structure. Consequently, most previous optimization strategies relied on slow coordinate descent strategies, which sequentially scan and query the modulation parameters one at a time. Our contribution lies in deriving an analytic method to compute the gradient of the wavefront shaping score directly from the scattered wavefront. Crucially, we can compute the gradient in closed-form, despite the unknown tissue structure. This analytic expression enables



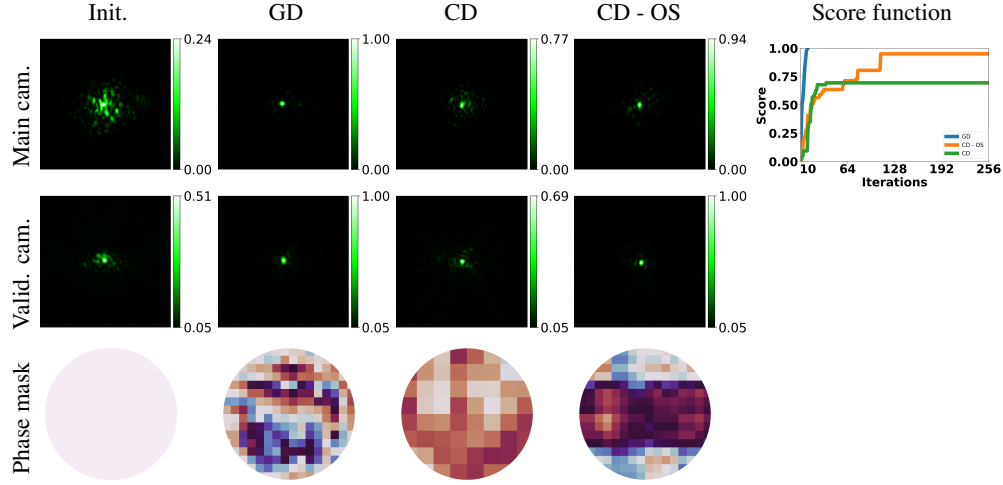


**Fig. 9. Comparison of gradient descent and coordinate descent schemes:** We compare our gradient descent (GD) optimization to coordinate descent (CD) using the Hadamard basis. Due to CD’s time-intensive nature, we optimize for a low-resolution mask and used a weak aberration volume (a single layer of parafilm tape). To address CD’s susceptibility to noisy measurements, we test two configurations: Standard CD where we used 5 shots to estimate the phase of each basis element. This approach could not improve the score beyond a certain point, because the improvement in the score is lower than the imaging noise. We next used an over-sampled CD (CD-OS) capturing twenty-four images per basis element. This over-sampled version is less susceptible to noise and reached a higher confocal score, at the cost of an even longer acquisition. Overall, our results demonstrate that GD converges significantly faster than both CD variants and exhibits greater robustness to noise.

transition from coordinate descent to gradient descent optimization, allowing simultaneous update to all SLM parameters at once. The resulting optimization strategy is orders of magnitude faster, a crucial factor for applications in dynamic media [65, 66]. Moreover, our approach facilitates the estimation of high-resolution modulations, potentially leading to superior corrections in more strongly scattering media.

We demonstrated the applicability of our gradient acquisition framework using a simple confocal-microscope setup. To enhance the utility of wavefront shaping corrections in real tissue imaging, our framework can be integrated into optical coherence tomography (OCT) or fluorescent microscope systems. OCT enables imaging deep within tissue volumes by isolating content at different depths through path-length filtering. However, in highly scattering tissues, OCT filtering is significantly affected by aberrations, which can be effectively corrected using a wavefront shaping system. Since OCT relies on coherent light, the optimization framework presented in this paper is directly applicable to OCT and can facilitate the development of a fast, aberration-corrected OCT system. Wavefront shaping is also highly effective in correcting the aberrations of fluorescence microscopes. In future work we plan to make a few modifications to the algorithm, and adapt it to incoherent light sources. The main challenge would be the low photon count emitted by fluorescent targets, and the low SNR with it will have to work.

Our rapid gradient-descent optimization algorithm resembles fast time-reversal algorithms [27, 30, 57–60] for wavefront shaping, which use the power iteration method to estimate the eigenvectors of the reflection matrix. The relationship with these algorithms is explored in detail in the



supplementary file. We demonstrate that when the target area includes a single point, our derived gradient is equivalent to a power iteration on the reflection matrix. However, as demonstrated in Fig. 4, for coherent imaging, the largest eigenvector of the reflection matrix does not always yield an optimal modulation and adjustments to the power iteration method often use ad-hoc approaches. In contrast, our approach of defining a target score and its gradient provides a more principled method for guiding the modulation search towards desired outcomes.

## 5. Methods

**System design:** Our setup is fully depicted in the supplementary Fig. 1. A collimated laser beam (CPS532 Thorlabs) illuminates a phase SLM (GAEA 2 Holoeye). The light is then focused with objective lens (N20X-PF Nikon) on the target plane through the scattering material. The reflected light from the target is collected through the same objective-lens and is modulated by a second SLM (LETO Holoeye). Finally the light is imaged with a camera (Atlas-314S Lucid vision labs). The second SLM (LETO Holoeye) has two functions: create phase pattern used for estimating the outgoing wavefront via a phase-retrieval algorithm. The second use is to place the conjugate of the retrieved phase in order to show confocal scanned images and calculate the score function. In our setup the SLMs are placed in the Fourier plane of the target. Additional details on the setup, calibration and alignment can be found in the supplementary material.

**Experimental targets:** For our targets we use high-reflecting chrome-coated chrome mask (Nanofilm) and use in-house lithography process to create pattern with a  $2\mu\text{m}$  resolution. For scattering material we used chicken breast tissue with thickness of  $130\mu\text{m} - 240\mu\text{m}$  or with a number of layers of parafilm [62], as stated in the text. For all targets chrome-mask results except for the results in Fig. 4 the target area for the algorithm was  $\mathcal{A} = 15.6\mu\text{m} \times 15.6\mu\text{m}$  and we scanned points inside this area at twice the Nyquist pitch, with a sampling interval of  $1.3\mu\text{m}$ . After the algorithm convergence the final confocal scan was done with a diffraction limited sampling interval of  $0.65\mu\text{m}$ . For the target on the fourth row of Fig. 5 the target spans over an area larger than  $\mathcal{A} = 15.6\mu\text{m} \times 15.6\mu\text{m}$ . Hence, we run the algorithm four times in partially overlapping areas and stitch the results together to form the final image.

For the bead targets in Fig. 6, since the beads are sparser we vary the target area so we image multiple beads. The target area for the  $3\mu\text{m}$  beads in the first two rows was  $\mathcal{A} = 16\mu\text{m} \times 16\mu\text{m}$  and  $\mathcal{A} = 32\mu\text{m} \times 32\mu\text{m}$ , respectively. The sampling interval was  $0.65\mu\text{m}$  for both algorithm and final confocal scan. For the  $0.5\mu\text{m}$  beads (rows 3-5) the area was  $\mathcal{A} = 13\mu\text{m} \times 13\mu\text{m}$  with sampling interval of  $0.5\mu\text{m}$  for both algorithm and final scan. We note that even if the beads are larger than the diffraction limit the expected non-aberrated image of the bead in a reflection confocal scanning is a diffraction-limited spot, since the beads act as a mini-lens [63]. Consequently,  $3\mu\text{m}$  beads appear as narrow isolated after our correction is applied.

For onion cell imaging, we employed a water-based gel as a medium between the microscope slide and the onion sample. This gel serves dual purposes: maintaining hydration of the onion cells and creating a sufficient gap between the sample and the microscope slide to mitigate reflections from the slide surface. The target area  $\mathcal{A} = 26\mu\text{m} \times 26\mu\text{m}$  with a sampling interval of  $1.3\mu\text{m}$ . To capture the full image we ran the algorithm seven times with partially overlapping areas and stitch the results together to form the final image.

In our current setup the run time of the algorithm is mainly limited by two components. The first is the liquid-crystal SLM, which works at rate of approximately  $17\text{Hz}$  for a phase pattern to fully transform. The second is performing gradient acquisition using phase diversity optimization. Each iteration of our algorithm requires acquiring five images for phase diversity optimization for each sampling direction, solving a phase diversity optimization problem for each sampling direction, and performing a gradient step using backtracking line-search (usually a single measurement is needed). For the results in Fig. 9 this means a runtime of 14 minutes. This is in comparison to coordinate-descent optimization which took 900 minutes in the same setup. By adding a

fast SLM (which currently run at  $1.4kH$ ) and using off-axis interferogram [7, 10, 13, 14, 16] runtime could be substantially decreased to mere seconds. In the supplementary material we further suggest an even faster setup using point-interferometry, we believe that with such a point diffraction interferometry implementation we can estimate a modulation in less than one second.

## References

1. A. D. Elliott, "Confocal microscopy: Principles and modern practices," *Curr. Protoc. Cytom.* **92**, e68 (2020).
2. A. Jr, A. Harris, J. Gross, *et al.*, "Optical coherence tomography angiography: An overview of the technology and an assessment of applications for clinical research," *Br. J. Ophthalmol.* **101** (2016).
3. W. Choi, C. Fang-Yen, K. Badizadegan, *et al.*, "Tomographic phase microscopy," *Nat. methods* **4**, 717–719 (2007).
4. Y. Choi, T. D. Yang, C. Fang-Yen, *et al.*, "Overcoming the diffraction limit using multiple light scattering in a highly disordered medium," *Phys. Rev. Lett.* (2011).
5. S. Kang, S. Jeong, W. Choi, *et al.*, "Imaging deep within a scattering medium using collective accumulation of single-scattered waves," *Nat. Photonics* **9**, 253–258 (2015).
6. A. Badon, V. Barolle, K. Irsch, *et al.*, "Distortion matrix concept for deep optical imaging in scattering media," *Sci. Adv.* (2020).
7. Y. Kwon, J. H. Hong, S. Kang, *et al.*, "Computational conjugate adaptive optics microscopy for longitudinal through-skull imaging of cortical myelin," *Nat. Commun.* **14**, 105 (2023).
8. S. Kang, Y. Kwon, H. Lee, *et al.*, "Tracing multiple scattering trajectories for deep optical imaging in scattering media," *Nat. communications* **14** (2023).
9. Y. Zhang, M. Dinh, Z. Wang, *et al.*, "Deep imaging inside scattering media through virtual spatiotemporal wavefront shaping," *arXiv preprint arXiv:2306.08793* (2024).
10. Y. Lee, D. Kim, Y. Jo, *et al.*, "Exploiting volumetric wave correlation for enhanced depth imaging in scattering medium," *Nat. communications* **14** (2023).
11. B. Y. Feng, H. Guo, M. Xie, *et al.*, "Neuws: Neural wavefront shaping for guidestar-free imaging through static and dynamic scattering media," *Sci. Adv.* **9**, eadg4671 (2023).
12. T. Yeminy and O. Katz, "Guidestar-free image-guided wavefront shaping," *Sci. Adv.* **7**, eabf5364 (2021).
13. O. Haim, J. Boger-Lombard, and O. Katz, "Image-guided computational holographic wavefront shaping," *Nat. Photonics* (2024).
14. P. Balondrade, V. Barolle, N. Guigui, *et al.*, "Multi-spectral reflection matrix for ultrafast 3d label-free microscopy," *Nat. Photonics* **18**, 1097–1104 (2024).
15. S. Kang, P. Kang, S. Jeong, *et al.*, "High-resolution adaptive optical imaging within thick scattering media using closed-loop accumulation of single scattering," *Nat. Commun.* **8**, 2157 (2017).
16. U. Najar, V. Barolle, P. Balondrade, *et al.*, "Harnessing forward multiple scattering for optical imaging deep inside an opaque medium," *Nat. Commun.* **15**, 7349 (2024).
17. L. Zhu, F. Soldevila, C. Moretti, *et al.*, "Large field-of-view non-invasive imaging through scattering layers using fluctuating random illumination," *Nat. Commun.* **13**, 1447 (2022).
18. Y. Baek, H. B. de Aguiar, and S. Gigan, "Phase conjugation with spatially incoherent light in complex media," *Nat. Photonics* **17**, 1114–1119 (2023).
19. S. Jeong, Y.-R. Lee, W. Choi, *et al.*, "Focusing of light energy inside a scattering medium by controlling the time-gated multiple light scattering," *Nat. Photonics* **12**, 277–283 (2018).
20. G. Weinberg, E. Sunray, and O. Katz, "Noninvasive megapixel fluorescence microscopy through scattering layers by a virtual incoherent reflection matrix," *Sci. Adv.* **10**, eadl5218 (2024).
21. Y. Jo, Y.-R. Lee, J. H. Hong, *et al.*, "Through-skull brain imaging in vivo at visible wavelengths via dimensionality reduction adaptive-optical microscopy," *Sci. Adv.* **8**, eabo4366 (2022).
22. N. Ji, "Adaptive optical fluorescence microscopy," *Nat. Methods* **14**, 374–380 (2017).
23. K. Hampson, R. Turcotte, D. Miller, *et al.*, "Adaptive optics for high-resolution imaging," *Nat. Rev. Methods Primers* **1**, 68 (2021).
24. R. Horstmeyer, H. Ruan, and C. Yang, "Guidestar-assisted wavefront-shaping methods for focusing light into biological tissue," *Nat. Photonics* **9**, 563–571 (2015).
25. H. Yu, J. Park, K. Lee, *et al.*, "Recent advances in wavefront shaping techniques for biomedical applications," *Curr. Appl. Phys.* **15**, 632–641 (2015).
26. S. Gigan, O. Katz *et al.*, "Roadmap on wavefront shaping and deep imaging in complex media," *J. Physics: Photonics* **4**, 042501 (2022).
27. C. Prada, J.-L. Thomas, and M. Fink, "The iterative time reversal process: Analysis of the convergence," *The J. Acoust. Soc. Am.* **97**, 62–71 (1995).
28. J. Jang, J. Lim, H. Yu, *et al.*, "Complex wavefront shaping for optimal depth-selective focusing in optical coherence tomography," *Opt. Express* **21**, 2890–2902 (2013).
29. A. Boniface, B. Blochet, J. Dong, and S. Gigan, "Noninvasive light focusing in scattering media using speckle variance optimization," *Optica* **6**, 1381–1385 (2019).
30. D. Aizik, I. Gkioulekas, and A. Levin, "Fluorescent wavefront shaping using incoherent iterative phase conjugation," *Optica* **9**, 746–754 (2022).

31. D. Aizik and A. Levin, "Non-invasive and noise-robust light focusing using confocal wavefront shaping," *Nat. communications* **15** (2024).
32. G. Stern and O. Katz, "Noninvasive focusing through scattering layers using speckle correlations," *Opt. Lett.* **44**, 143 (2018).
33. O. Katz, E. Small, Y. Guan, and Y. Silberberg, "Noninvasive nonlinear focusing and imaging through strongly scattering turbid layers," *Optica* **1**, 170–174 (2014).
34. I. M. Vellekoop and A. P. Mosk, "Focusing coherent light through opaque strongly scattering media," *Opt. Lett.* **32**, 2309–2311 (2007).
35. D. B. Conkey, A. N. Brown, A. M. Caravaca-Aguirre, and R. Piestun, "Genetic algorithm optimization for focusing through turbid media in noisy environments," *Opt. Express* **20**, 4840 (2012).
36. S. M. Popoff, G. Lerosey, R. Carminati, *et al.*, "Measuring the transmission matrix in optics: An approach to the study and control of light propagation in disordered media," *Phys. Rev. Lett.* **104**, 100601 (2010).
37. I. M. Vellekoop, A. Lagendijk, and A. P. Mosk, "Exploiting disorder for perfect focusing," *Nat. Photonics* **4**, 320–322 (2010).
38. Z. Yaqoob, D. Psaltis, M. S. Feld, and C. Yang, "Optical phase conjugation for turbidity suppression in biological samples," *Nat. Photonics* **2**, 110–115 (2008).
39. Y. Chen, M. K. Sharma, A. Sabharwal, *et al.*, "3PointTM: Faster measurement of high-dimensional transmission matrices," in *Euro. Conf. Computer Vision (ECCV)*, (2020).
40. J. Tang, R. N. Germain, and M. Cui, "Superpenetration optical microscopy by iterative multiphoton adaptive compensation technique," *Proc. Natl. Acad. Sci.* **109**, 8434–8439 (2012).
41. C. Wang, R. Liu, D. E. Milkie, *et al.*, "Multiplexed aberration measurement for deep tissue imaging in vivo," *Nat. Methods* **11**, 1037–1040 (2014).
42. T. L. Liu, S. Upadhyayula, D. E. Milkie, *et al.*, "Observing the cell in its native state: Imaging subcellular dynamics in multicellular organisms," *Science* **360**, eaaq1392 (2018).
43. R. Fiolka, K. Si, and M. Cui, "Complex wavefront corrections for deep tissue focusing using low coherence backscattered light," *Opt. Express* **20**, 16532–16543 (2012).
44. X. Xu, H. Liu, and L. Wang, "Time-reversed ultrasonically encoded optical focusing into scattering media," *Nat. Photonics* **5**, 154–157 (2011).
45. Y. M. Wang, B. Judkewitz, C. A. DiMarzio, and C. Yang, "Deep-tissue focal fluorescence imaging with digitally time-reversed ultrasound-encoded light," *Nat. Commun.* **3**, 928 (2012).
46. F. Kong, R. H. Silverman, L. Liu, *et al.*, "Photoacoustic-guided convergence of light through optically diffusive media," *Opt. Lett.* **36**, 2053–2055 (2011).
47. I. M. Vellekoop, M. Cui, and C. Yang, "Digital optical phase conjugation of fluorescence in turbid tissue," *Appl. Phys. Lett.* **101**, 081108 (2012).
48. S. M. Popoff, A. Aubry, G. Lerosey, *et al.*, "Exploiting the time-reversal operator for adaptive optics, selective focusing, and scattering pattern analysis," *Phys. Rev. Lett.* **107**, 263901 (2011).
49. J. Mertz, H. Paudel, and T. G. Bifano, "Field of view advantage of conjugate adaptive optics in microscopy applications," *Appl. Opt.* (2015).
50. M. Alterman, C. Bar, I. Gkioulekas, and A. Levin, "Imaging with local speckle intensity correlations: theory and practice," *ACM TOG* (2021).
51. G. Osnabrugge, R. Horstmeyer, I. N. Papadopoulos, *et al.*, "Generalized optical memory effect," *Optica* **4**, 886–892 (2017).
52. B. H. Dean and C. W. Bowers, "Diversity selection for phase-diverse phase retrieval," *J. Opt. Soc. Am. A* **20**, 1490–1504 (2003).
53. R. A. Gonsalves, "Phase Retrieval And Diversity In Adaptive Optics," *Opt. Eng.* **21**, 215829 (1982).
54. E. J. Candes, X. Li, and M. Soltanolkotabi, "Phase retrieval via wirtinger flow: Theory and algorithms," *IEEE Transactions on Inf. Theory* **61**, 1985–2007 (2015).
55. R. N. Smartt and W. H. Steel, "Theory and application of point-diffraction interferometers," *Jpn. J. Appl. Phys.* **14**, 351 (1975).
56. V. Akondi, A. Jewel, and B. Vohnsen, "Digital phase-shifting point diffraction interferometer," *Opt. Lett.* **39**, 1641–4 (2014).
57. H. C. Song, W. A. Kuperman, W. S. Hodgkiss, *et al.*, "Iterative time reversal in the ocean," *The J. Acoust. Soc. Am.* **105**, 3176–3184 (1999).
58. H. Ruan, M. Jang, B. Judkewitz, and C. Yang, "Iterative time-reversed ultrasonically encoded light focusing in backscattering mode," *Sci. reports* **4**, 7156 (2014).
59. K. Si, R. Fiolka, and M. Cui, "Breaking the spatial resolution barrier via iterative sound-light interaction in deep tissue microscopy," *Sci. reports* **2**, 748 (2012).
60. I. Papadopoulos, J.-S. Jouhannau, J. Poulet, and B. Judkewitz, "Scattering compensation by focus scanning holographic aberration probing (f-sharp)," *Nat. Photonics* (2016).
61. C. K. Mididoddi, R. J. Kilpatrick, C. Sharp, *et al.*, "Threading light through dynamic complex media," *Nat. Photonics* **19**, 123–134 (2025).
62. A. Boniface, J. Dong, and S. Gigan, "Non-invasive focusing and imaging in scattering media with a fluorescence-based transmission matrix," *Nat. Commun.* (2020).

63. W. Weise, P. Zinin, T. Wilson, *et al.*, "Imaging of spheres with the confocal scanning optical microscope," *Opt. Lett.* **21**, 1800–1802 (1996).
64. W. Wang and C. Li, "Measurement of the light absorption and scattering properties of onion skin and flesh at 633nm," *Postharvest Biol. Technol.* **86**, 494–501 (2013).
65. I. M. Vellekoop, "Feedback-based wavefront shaping," *Opt. Express* **23**, 12189–12206 (2015).
66. L. Valzania and S. Gigan, "Online learning of the transmission matrix of dynamic scattering media," *Optica* **10**, 708–716 (2023).

# Rapid wavefront shaping using an optical gradient acquisition-supplementary material

## 1. OPTICAL SYSTEM

**System:** A drawing of our system is shown in Fig. S1. A collimated laser passes through a polarizer to align the laser polarization with the SLM main-axis and then expanded with a beam-expander (L1-L2). The wavefront is then modulated by the illumination-SLM and reflected towards the sample. The modulated light passes through an objective lens and illuminates the sample. The forward scattering light continues to the validation camera which is used for validating focus of our algorithm on the image plane. The reflected light from the sample returns through the same objective lens and is reflected at a beam-splitter towards the imaging-SLM which again modulates the wavefront. Finally the light is collected by the main-camera sensor. The imaging-SLM has two functions: The first is to present the optimized pattern  $u^l(\rho)$  when measuring the score function and when confocal scanning a target. The second function is to present different defocus phase functions for capturing patterns for phase diversity optimization.

A full component list of our system: 532nm laser (CPS532 Thorlabs), P - linear polarizer (LPNIRB100 Thorlabs), L1 - 100mm achromatic lens, L2 - 400mm achromatic lens, L3 - 150mm achromatic lens, L4 - 100mm achromatic lens, L5 - 200mm achromatic lens, TL - tube lens (TTL200-A Thorlabs), BS - beamsplitter (62-882 Edmund), OL1 - objective lens NA=0.5, MAG= $\times 20$  (N20X-PF Nikon), OL2 - objective lens NA=0.7, MAG= $\times 100$  (MY100X-806 Mitutoyo). Lens translation stage is a single-axis stage (PT1 Thorlabs) with a motorized actuator (Z925B Thorlabs). The sampler holder was custom created with three translation stages (PT1 Thorlabs) allowing to adjust the target in all three-axes. For the main camera we use A314S Atlas (Lucid vision) and for the validation camera we use Grasshopper3 USB3 (Teledyne Flir).

**System alignment:** We start by explaining how we align our system. To modulate the Fourier transform of the wave the illumination-SLM needs to be at the focal plane of the lens following it (L3 in Fig. S1), and the imaging-SLM at the focal plane of the lens before it (same L3). We perform this alignment by using a third camera focused at infinity (we place an appropriate laser line filter (532nm) and focus the camera at a far building). Then we place two polarizers: before the SLM at degree of  $45^\circ$  and after the SLM at degree of  $135^\circ$ . Putting the polarizers in these angles convert the phase modulation to intensity variation (dark pixel of the SLM pixel if it does not modulate the light and on a white pixel if it modulates by  $\pi$ ). We then focus on the SLM through the relevant lens, forming a relay system. We display a checkerboard pattern on the SLM and adjust the distance between the SLM and the lens until we get a sharp image. We also calibrate the distance between the main/validation cameras and the lenses before them (L4/L5) to ensure they are focused at infinity.

**Finding the active SLM area:** After the system is aligned, we find the relevant area on both SLMs which are illuminated and pass through the objective lens aperture. The relevant area size can be calculated based on the size of the aperture and pixel size. We describe how we calibrate the illumination-SLM and the imaging-SLM follows a similar procedure. In order to find the center  $(x_c, y_c)$  we use the following procedure: We start by placing a mirror on the sample holder and move the sample holder until we achieve focus at the main-camera. To get an initial estimate of the centers we present a sinusoidal pattern of the same size of the aperture on the SLM and move it on  $x - y$  axes of the SLM and look when we get a maximum intensity at the target pixel (if we do not modulate the right area on the SLM less light is directed to that target pixel), this gives us an initial estimate of  $(x_e, y_e)$ . We then place a defocus pattern (quadratic phase  $((x - (x_c - x_e))^2 + (y - (y_c - y_e))^2)$ ) on the illumination SLM and move the sample holder axially until again we achieve focus on the main-camera. Ideally if  $(x_c, y_c) = (x_e, y_e)$  the location of the laser spot will be at the same  $x - y$  location no matter what quadratic phase we introduce. If the location of the laser spot is different we modify our estimation. We repeat this until the focus does not change. This is then repeated for the imaging-SLM while the illumination-SLM

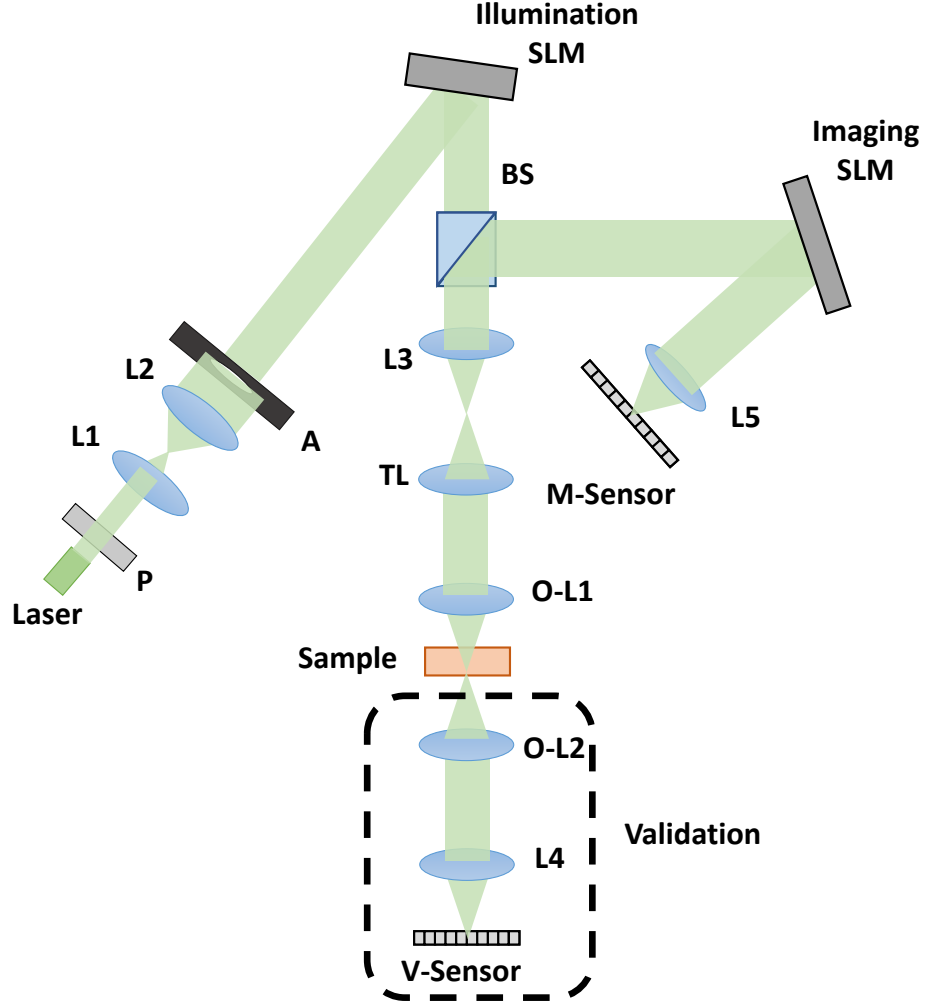


**Fig. S1. Setup:** we present the full setup of optical system. Light emitted by the laser is reflected from the illumination-SLM towards the sample. The reflected light from the sample returns through the same path where it is reflected from the imaging-SLM and is then collected by the main-sensor. The transmitted light from the sample continues to the validation sensor which is only used to validate our results. P:polarizer, BS:beam-splitter, L-lens, O-L:objective lens, V-sensor:Validation sensor, M-Sensor:Main sensor.

presents blank phase.

**Mapping of SLM to camera:** Next, we calibrate the mapping between the SLMs and the main camera. Using the focal length of the lens before the camera (L5), the SLM pitch and the wavelength of the emitted light, we can map between SLM frequencies to the camera pixel using simple geometry. However, this mapping does not account for misalignment in rotation of the SLMs. To overcome this we fine-tune the calibration by displaying sinusoidal patterns and recording the shift presented on the main camera. Using these measurements we estimate the rotation of the SLM.

**Mapping between SLMs:** Finally, we need an to be able to accurately map every pixel on the illumination SLM to the corresponding pixel on the camera SLM. To do this we follow a similar procedure as in [1, 2], where instead of a using a fluorescent bead we illuminate the target from the back bypassing the L-SLM i.e. we place mirrors so the laser is directed through O-L2 and after the sample the light continues to main camera, as shown in Fig. S2. We then recover the modulation pattern by applying phase-diversity optimization. The Helmholtz reciprocity (phase

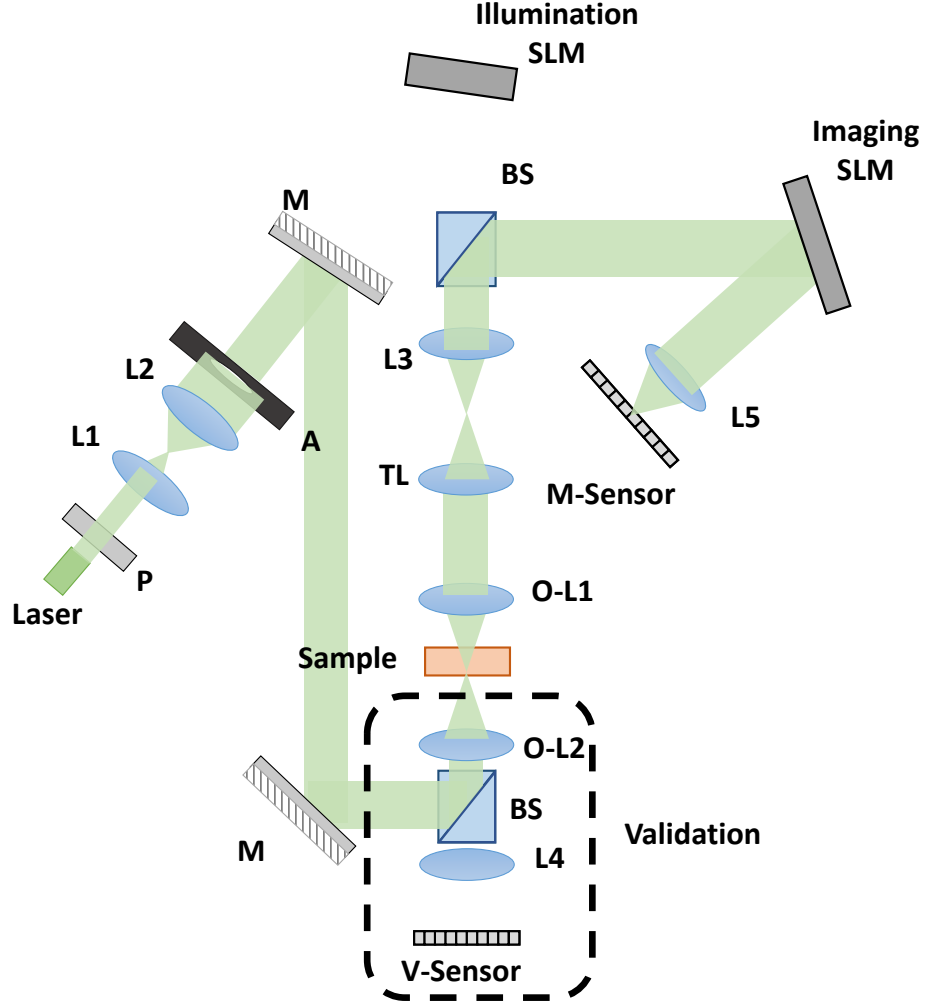


**Fig. S2. Back calibration:** We use a back-path laser to calibrate our system, here we show that laser path using back-path.

conjugation) principle [3] dictates that if we place the conjugate of the recovered wavefront on the illumination-SLM, it will focus into a point behind the scattering tissue. Hence, we redirect the laser to the forward path Fig. S1 (i.e. through the illumination-SLM and O-L1) and place the modulation pattern on illumination-SLM and we expect to achieve a focused point on the validation camera. However, if the mapping between the SLMs is wrong we don't get a focused point on the validation camera. Now we can find the mapping between the SLMs by shifting the pattern on the illumination-SLM until the energy on the focused point on the validation camera is maximum.

**Tilt-shift parameter calibration:** As our score maximizes the confocal intensity over an area we rely on the tilt shift memory effect. To apply the scan we need to recover the parameter determining the ratio between the tilt and shift. To determine this parameter we again follow a similar calibration method as [1, 2]; however, since they rely on fluorescent beads we again illuminate the target by illuminating the target from the back bypassing the L-SLM. We then recover the modulation pattern by applying phase-diversity optimization. We then redirect the laser to the forward path (i.e. through the illumination-SLM and O-L1) and place the modulation pattern on illumination-SLM and we use the validation camera to view the focused spot. We then adjust the ratio between tilt and shift of the modulation pattern so that we can move the focused spot in the validation camera, while preserving maximal intensity.

**Gradient step:** When performing gradient descent optimization we need to choose a step-size at each iteration. In our system, we use backtracking line search [4]. For each iteration we start with a predefined step size and after performing a step we measure the score function. If the score function increases we perform the step; however, if the score decreases we do not perform the step. Instead we divide the step size by two and again measure the score. We repeat this until the score increases or until the step size is smaller than some threshold. If the score does not increase we perform a large step (with the initial step size) as the optimization might be stuck in a local-maximum. At the end of optimization we choose the phase modulation pattern that scored the highest score.

## 2. JUSTIFYING THE CONFOCAL AREA SCORE

To find good wavefront shaping modulation our algorithm relies on a score function, measuring the confocal intensity over a small area  $\mathcal{A}$ . For that we scan the area by tilting and shifting the modulation toward a point  $\ell \in \mathcal{A}$  and collect the averaged confocal intensity:

$$S(\rho) \equiv \sum_{\ell \in \mathcal{A}} |\mathbf{u}^\ell(\rho)^T \mathcal{R} \mathbf{u}^\ell(\rho)|^2. \quad (\text{S1})$$

This score was used by a number of recent approaches for digital aberration correction [5–7]. They optimize over finite isoplanatic patches to maximize the diagonal elements of the reflection matrix, and the sum of these diagonal elements is equivalent to our confocal area score. To better explain why this score favors focusing wavefront-shaping modulations, we provide a derivation below. For that let us denote by  $\mathcal{T}$  the transmission matrix describing the propagation of light from the SLM plane to a mirror attached at the back of the scattering volume. It has been shown that the reflection matrix can be expressed as a double pass through the transmission matrix [5, 6, 8]

$$\mathcal{R} = \mathcal{T}^T \cdot \mathcal{T}, \quad (\text{S2})$$

where  $\mathcal{T}^T$  is the transpose of the transmission matrix (this is just transpose, not a conjugate transpose).

We now consider an incoming modulation  $\mathbf{u}^\ell(\rho)$  and denote the complex wavefront it generates at the back of the tissue as

$$\mathbf{v}^\ell = \mathcal{T} \mathbf{u}^\ell(\rho). \quad (\text{S3})$$

We will express the confocal area score using the wavefront at the back layer and show that under idealized memory effect correlation, this score is equivalent to the nonlinear score of two-photon fluorescent excitation [9], or the single photon confocal fluorescent feedback [1]. It has already been shown that such a score is maximized by focusing modulations, namely, when  $\mathbf{v}$  is a one-hot vector that brings all the energy into a single point and has zero intensity over the rest of its entries.

**Claim 1.** Let  $\mathbf{v}^o = \mathcal{T} \mathbf{u}^o(\rho)$  denote the wavefront at the back of the tissue where the incoming illumination is directed to a point  $\ell_o$  at the center of the patch  $\mathcal{A}$ . If memory effect correlation holds over the area  $\mathcal{A}$ , the confocal area score of Eq. (S1) reduces to:

$$S(\rho) = \sum_x |\mathbf{v}^o(x)|^4, \quad (\text{S4})$$

where  $x$  is a 2D position vector, running over the coordinates of  $\mathbf{v}^o$ .

*Proof.* The confocal intensity resulting from one modulation tilted toward point  $\ell$  can be expressed as

$$I^\ell(0) = \left| \sum_x (\mathbf{v}^\ell(x))^2 \right|^2, \quad (\text{S5})$$

where  $x$  runs over points on the back plane of the tissue, and at each such point we square the complex field while maintaining its phase (this is not an absolute value). The confocal area score can then be expressed as

$$S(\rho) = \sum_\ell I^\ell(0) = \sum_\ell \left| \sum_x (\mathbf{v}^\ell(x))^2 \right|^2 \quad (\text{S6})$$



We now use the tilt-shift memory effect [10, 11] that states that if we tilt the incoming modulation towards two points  $\ell$  and  $\ell_o$  (where  $\ell_o$  denotes the center of the patch, and  $\ell$  is another point in  $\mathcal{A}$ ) separated by a 2D displacement vector  $\Delta_\ell = \ell - \ell_o$ , then the fields at the back of the tissue satisfy a tilt-shift correlation and

$$\mathbf{v}^\ell(x) \approx \mathbf{v}^o(x + \Delta_\ell) e^{\frac{2\pi i}{\lambda L} (\Delta_\ell \cdot x)}, \quad (\text{S7})$$

where  $L$  is 2/3 of the tissue thickness. Assuming the memory effect correlation is strong enough, we can use the wavefront  $\mathbf{v}^o$  generated when directing light to the center of the patch  $\mathcal{A}$ , and express all other wavefronts  $\mathbf{v}^\ell$ , generated when directing light to the rest of the patch. With this, we can express the confocal area score of Eq. (S6) as

$$\mathcal{S}(\rho) = \sum_\ell \left| \sum_x (\mathbf{v}^o(x))^2 e^{\frac{2\pi i}{\lambda L} (\Delta_\ell \cdot x)} \right|^2. \quad (\text{S8})$$

Expanding Eq. (S8) we can write

$$\mathcal{S}(\rho) = \sum_{x_1, x_2} (\mathbf{v}^o(x_1))^2 \cdot (\mathbf{v}^o(x_2))^* \sum_\ell e^{\frac{2\pi i}{\lambda L} (\Delta_\ell \cdot (x_1 - x_2))} \quad (\text{S9})$$

We now note that if  $x_1 \neq x_2$  and the range of  $\Delta_\ell$  values is large enough terms of the form  $\sum_\ell e^{\frac{2\pi i}{\lambda L} (\Delta_\ell \cdot (x_1 - x_2))}$  are equivalent to the mean of a sinusoidal, which is 0. Therefore, Eq. (S10) reduces to

$$\mathcal{S}(\rho) = \sum_x |\mathbf{v}^o(x)|^4, \quad (\text{S10})$$

as desired.  $\square$

**Claim 2.** *Assuming sufficient memory effect correlation, the confocal area score is maximized when the incoming modulation  $\rho$  makes the wavefront  $\mathbf{v}$  at the back of the tissue a sparse one-hot vector.*

*Proof.* Using the previous claim, the confocal area score is equivalent to  $\mathcal{S}(\rho) = \sum_x |\mathbf{v}^o(x)|^4$ . This is equivalent to the confocal score one measures using incoherent fluorescent wavefront shaping [1] with single photon excitation, or to the nonlinear emission using two photon excitation [9], and it has already been shown that this score favors focusing modulations. To see this, note that the total laser power is bounded and by using a modulation we can spread the light in different ways, but we cannot increase its power. Therefore, for any modulation  $\rho$  the norm of the wavefront  $\mathbf{v}^o$  behind the tissue is bounded, and

$$\sum_x |\mathbf{v}^o(x)|^2 \leq C. \quad (\text{S11})$$

It is easy to see that to maximize  $|\mathbf{v}^o(x)|^4$  under the bounded norm constraint, it is best if  $\mathbf{v}^o$  is a one-hot vector that has all its power in one entry and zero energy at all other entries.  $\square$

**Tilt-shift and time reversal:** Our algorithm optimizes the wavefront to ensure that input and output fields are similar and exhibit the memory effect, and ensure that focusing on adjacent points results in tilt-shifted versions of each other. To illustrate this, we present simulation results of our algorithm in Fig. S3. Assuming the SLM is conjugate to the output plane, we demonstrate the focusing achieved for two spots inside the tissue before and after applying our algorithm.

We simulate a scenario without applying wavefront correction and present the intensity on the imaging plane. In this case, light is aberrated and spread across the target plane. This results in an uncorrelated reflected wavefront returning to the SLM plane  $u_{out}^{w/o}$ , when compared with the conjugate phase presented on the SLM  $u_{in}^{w/o}$ , with correlation score:  $C(u_{in}^{w/o}, u_{out}^{w/o}) = 0.51$ . Additionally, since light reflects from a large area inside the tissue, wavefronts reflected from two different points  $u_{out_c}^{w/o}, u_{out_l}^{w/o}$  are also uncorrelated, with  $C(u_{out_c}^{w/o}, u_{out_l}^{w/o}) = 0.47$ .

Conversely, after applying our algorithm to optimize a wavefront that incorporates both memory effect and time-reversal principle, we achieve focus on the target plane. This improvement is exhibited by increased correlation between incoming SLM modulation and output wavefronts  $C(u_{in}^{w/}, u_{out}^{w/}) = 0.87$ , as well as enhanced correlation between wavefronts reflected by neighboring points on the target plane  $C(u_{out_c}^{w/}, u_{out_l}^{w/}) = 0.77$ .

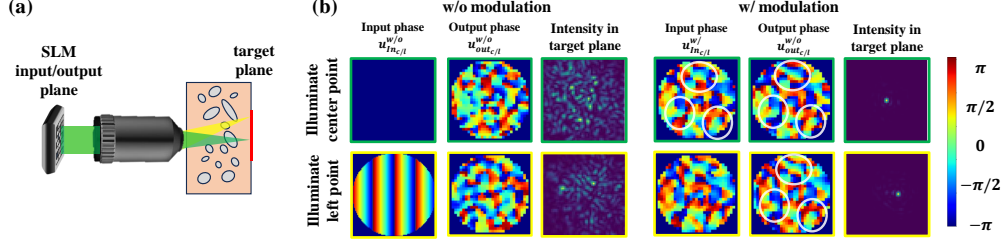


**Fig. S3. Tilt-shift and time reversal effects:** (a) We show a simplified schematic of our system with two input wavefronts, green focusing into the center of the imaging plane and yellow focusing to a neighboring point to the left. (b) Simulation results showing the incoming phase on the SLM, the conjugate of the output phase after tissue reflection (when reaching the SLM plane), and the intensity at the target plane. With light modulation, strong correlations are observed between the incoming SLM phase and the output phase, as well as between output phases for different points (white circles indicate areas of strong correlation). Without aberration correction, correlation decreases rapidly.

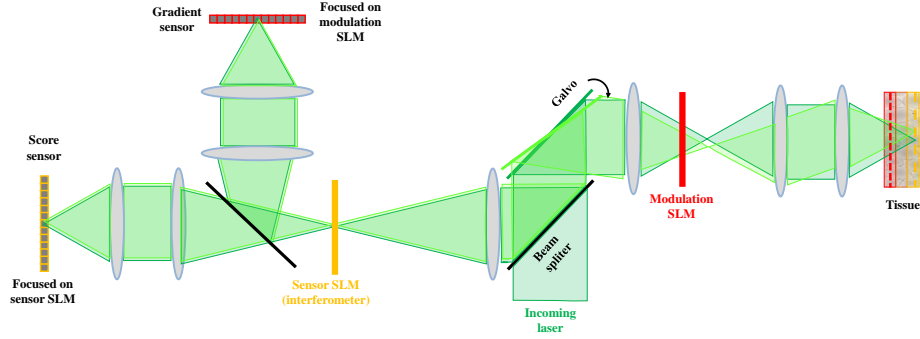


**Fig. S4. Setup for interferometric gradient acquisition:** An incoming laser beam is directed to focus on a point inside the tissue, the focal point can be shifted with a galvo. The figure illustrates two such tilted paths in two shades of green. On its way to the sample the beam passes through a relay system, containing an SLM for aberration correction. The SLM is placed such that it is conjugate to a plane inside the tissue volume. Another SLM is used as an interferometer to modulate the reflected light captured by the sensor. Two cameras are used in this setup - the first is focused on the interferometer SLM and termed score sensor. The second sensor is focused on the modulation SLM and termed gradient sensor.

### 3. GRADIENT ACQUISITION

#### A. Gradient acquisition using phase diversity optimization

To acquire the gradient of our wavefront shaping score, we need to capture the complex wavefront arriving at the sensor  $\mathbf{v}^\ell = \mathcal{R}\mathbf{u}^\ell(\rho)$ , for every point  $\ell$  in the scanned area  $\mathcal{A}$ . In our current implementation, we do this using a phase diversity optimization scheme [12, 13], for each of the target points. That is, we sequentially place the modulation wavefronts  $\mathbf{u}^\ell(\rho)$  on the illumination SLM and capture the resulting speckle intensity images at the sensor. We place on the camera SLM 5 known defocus wavefronts  $\mathbf{u}_{\text{defocus}}^j$  and capture 5 speckle intensity images  $I_\ell^1, \dots, I_\ell^5$ . We use these images to solve an optimization problem retrieving the phase of the complex wavefront from the measured intensity images [14], resulting in the optimization problem:

$$\hat{\mathbf{v}}^\ell = \arg \max_{\mathbf{v}^\ell} \sum_{j=1}^5 \left\| I_\ell^j - |\mathcal{F}(\mathbf{v}^\ell \odot \mathbf{u}_{\text{defocus}}^j)|^2 \right\|^2. \quad (\text{S12})$$

We scan multiple points  $\ell \in \mathcal{A}$  and repeat the same phase optimization. These wavefronts are

averaged to compute one instance of the gradient.

$$\mathcal{R}\mathbf{u}^\ell(\rho) = \mathbf{v}_{\text{estimate}}^\ell = \frac{1}{\mathcal{A}} \sum_{\ell \in \mathcal{A}} \mathbf{v}^\ell. \quad (\text{S13})$$

### B. Fast gradient acquisition using point diffraction interferometry

We describe another future approach for gradient acquisition which would allow us to acquire it much faster, using a small number of only 3 shots. This possible setup would utilize a variant of a point diffraction interferometry system [15, 16], that can capture the complex wavefront with no optimization, and can also average over all  $\ell \in \mathcal{A}$  within one shot.

**Setup for point diffraction interferometry:** Fig. S4 illustrates a setup for gradient acquisition with point diffraction interferometry. A laser beam illuminates a tissue sample, and an SLM can modulate its shape. The SLM is placed such that it is conjugate to a plane inside the tissue, where the aberration is actually happening. The illumination wavefront propagates through the scattering tissue, reflects from its internal structure and back-scatters to the camera. The returning light passes through the same SLM on its way to the camera. The returning modulated light splits at a beam splitter toward two sensors. Before the sensors, the light passes through another relay system and a second SLM. This second SLM is placed such that it is conjugate to the target we wish to image rather than conjugate to the aberration plane. We refer to the first SLM (closer to the sample) as “the modulation SLM” and to the second one as “the sensor SLM”. After the sensor SLM the light splits through another beam-splitter toward two sensors. The first sensor (which can also be a single point detector) is placed such that it is conjugate to the target points we wish to image and to the sensor SLM, and would measure the confocal intensity score at the center of the frame. The second 2D sensor is placed such that it is conjugate to the modulation SLM and would measure the gradient directly. We refer to these two sensors as the *score sensor*, and the *gradient sensor*.

The setup also includes a galvo that can tilt the incoming and outgoing light. While we can implement such a tilt with the SLM itself, a galvo can be tilted faster than the refresh rate of the SLM. By tilting the incoming beam we can direct it toward different target points  $\ell \in \mathcal{A}$ . Tilting the returning beam implies that the light scattered from target point  $\ell$  is directed to the central pixel of the sensor, regardless of the actual spatial position of  $\ell$ . In this setup, to illuminate the tissue with the modulation wavefront  $\mathbf{u}^\ell(\rho)$ , we place  $\rho$  on the SLM and use the galvo to tilt it toward the target point  $\ell$ , so effectively we get:

$$\mathbf{u}^\ell(\rho)(x) = \zeta_x \odot e^{\frac{2\pi i}{\lambda}(\tau^\ell \cdot x)} \odot \rho(x), \quad (\text{S14})$$

where  $\tau^\ell$  represents the tilt toward point  $\ell$ .  $\zeta_x$  represents here the shape of the illumination wavefront reaching the modulation SLM. Since our SLM is not placed at the Fourier plane of the system, it is illuminated by a spherical wavefront and not by a plane wave. Note that  $\zeta_x$  was defined in the main paper as the (known) propagation of the wavefront from the modulation SLM to the center of the sensor, since we assume our system is fully symmetric the same  $\zeta_x$  applies both on the incoming and on the outgoing paths.

**Interferometric measurements:** We start with a mathematical expression for the wavefront we will measure by the gradient sensor. We recall that this sensor is focused at the modulation SLM and directly images the wavefront at this plane. If we use a flat phase on the sensor SLM, and display the modulation  $\mathbf{u}^\ell(\rho)$  (by displaying  $\rho$  on the modulation SLM and combining it with the proper galvo tilt), it will measure the 2D wavefront

$$\mathbf{v}^\ell = \left( \mathbf{u}^\ell(\rho) \right) \odot \left( \mathcal{R}\mathbf{u}^\ell(\rho) \right), \quad (\text{S15})$$

where  $\mathcal{R}\mathbf{u}^\ell(\rho)$  is the propagation of the incoming modulated illumination via the tissue and back to the SLM plane. On the SLM plane, each coordinate is multiplied again by  $\mathbf{u}^\ell(\rho)$ . We use the notation  $\odot$  to denote an element-wise multiplication between two 2D fields. Since we image the modulation SLM plane we measure this as a 2D wavefront and not as a scalar.

Next, denote by  $\mu^\ell$  the complex scalar reaching the center of the score sensor, when there is a blank phase on the sensor SLM. As this sensor is focused on the target plane (and on the sensor SLM, which is conjugate to the target plane):

$$\mu^\ell = (\mathbf{u}^\ell(\rho))^T \mathcal{R}\mathbf{u}^\ell(\rho), \quad (\text{S16})$$

where  $\mathbf{u}^\ell(\rho)$  is defined in Eq. (S14) to include the SLM modulation, the tilt, and the propagation from the modulation plane to the score sensor.

If we could place an aperture on pixel  $x$  of the 2nd sensor SLM (so we block the parts of the wavefront that do not pass via point  $x$ ), the 2D wavefront we measure at the gradient sensor (which is focused on the modulation SLM) is governed by the scalar  $\mu^\ell$  and corresponds to

$$\mathbf{v}_1^\ell = \mu^\ell \cdot \zeta_x^*, \quad (\text{S17})$$

where  $\zeta_x$ , defined in Eq. (2) of the main paper encodes the (known) propagation from the modulation SLM plane to the center of the score sensor. We denote the difference between the wavefronts in Eq. (S15) and Eq. (S17) by

$$\mathbf{v}_2^\ell = \mathbf{v}^\ell - \mathbf{v}_1^\ell. \quad (\text{S18})$$

Moreover, rather than using a pinhole on the sensor SLM, we suggest to vary the phase of pixel  $x$  of the sensor SLM to  $\phi_j$  while keeping all other pixels at phase 0. This implies that the gradient sensor would see the wavefront  $\mathbf{v}_2^\ell + e^{i\phi_j} \mathbf{v}_1^\ell$ , where  $\mathbf{v}_2^\ell$  is the part of the wavefront that passes when blocking pixel  $x$ , and  $e^{i\phi_j} \mathbf{v}_1^\ell$  is the part that passed via pixel  $x$  after its phase is adjusted. We can use standard phase shifting interferometry and measure  $J = 3$  intensity images while varying the phase  $\phi_j$  of the central pixel equally between 0 and  $2\pi$ . We measure

$$I_j^\ell = |\mathbf{v}_2^\ell + e^{i\phi_j} \mathbf{v}_1^\ell|^2 = e^{-i\phi_j} \mathbf{v}_1^{\ell*} \mathbf{v}_2^\ell + e^{i\phi_j} \mathbf{v}_1^\ell \mathbf{v}_2^{\ell*} + |\mathbf{v}_1^\ell|^2 + |\mathbf{v}_2^\ell|^2. \quad (\text{S19})$$

By summing the intensity images with the corresponding phase we can isolate the interference term

$$\mathbf{v}_1^{\ell*} \mathbf{v}_2^\ell = \sum_j e^{i\phi_j} I_j^\ell. \quad (\text{S20})$$

We can also measure  $|\mathbf{v}_1^\ell|^2$  and add it to Eq. (S20) to receive

$$\mathbf{g}^\ell = \mathbf{v}_1^{\ell*} \mathbf{v}^\ell. \quad (\text{S21})$$

We can now substitute Eqs. (S14), (S15) and (S17), and check the content of this interference term:

$$\mathbf{g}^\ell = \mu^{\ell*} \cdot (\zeta_x \odot \mathbf{u}^\ell(\rho)) \odot (\mathcal{R}\mathbf{u}^\ell(\rho)) \quad (\text{S22})$$

$$= \underbrace{\mu^{\ell*}}_{(1)} \cdot \underbrace{\zeta_x \odot \rho}_{(2)} \odot \underbrace{\zeta_x \odot e^{\frac{2\pi i}{\lambda}(\tau^\ell \cdot x)}}_{(3)} \odot \underbrace{(\mathcal{R}\mathbf{u}^\ell(\rho))}_{(4)}. \quad (\text{S23})$$

Comparing this formula to the gradient derived in Eq. (5) of the main paper, we see that it corresponds to the desired gradient up to known multiplicative terms. Term (1) corresponds to term (1) of the gradient, term (2) is a known multiplicative factor, term (3) is effectively the derivative of the tilted modulation  $\mathbf{u}^\ell(\rho)$  with respect to the SLM parameters  $\frac{\partial \mathbf{u}^\ell(\rho)}{\partial \rho}$ , which is term (3) in Eq. (5) of the main paper, see definition in Eq. (S14). Term (4) is equivalent to term (2) in Eq. (5) of the main paper.

Moreover, note that to average over target points  $\ell \in \mathcal{A}$  all we need to do is to scan the galvo toward a different direction, without changing the pattern  $\rho$  on the SLM. This effectively implies that we can tilt the galvo *within exposure*, and capture 3 speckle images

$$I_j = \sum_\ell I_j^\ell. \quad (\text{S24})$$

From these 3 images we can compute the gradient directly.

The above derivation suggests a possible future implementation of our wavefront shaping algorithm, that will allow us to image the gradient of the confocal score directly, using as little as 3 shots, where the scanning over the target area is done within exposure. Furthermore since we use an interferometer no phase diversity optimization is required and the complex wavefront is measured directly.

#### 4. EQUIVALENCE TO POWER ITERATIONS

The gradient derived above is similar to rapid time reversal based approach for wavefront shaping [2, 17–21]. Similar ideas were also used by digital correction algorithms [5, 22, 23]. These approaches start from the assumption that the desired modulation is the largest eigenvector of the reflection (or transmission) matrix of the tissue. This eigenvector can be estimated very efficiently using power iterations. In each iteration, one displays a modulation  $\mathbf{u}$  on the SLM, measures  $\mathcal{R}\mathbf{u}$  and uses it as the next guess for the modulation.

We argue that the gradient we derived above collapses to such a power iteration, if we restrict our score function on an area  $\mathcal{A}$  consisting of a single target point  $\ell$ . To see note that if we attempt to maximize the score

$$\mathcal{S}(\boldsymbol{\rho}) = \left| \mathbf{u}^\ell(\boldsymbol{\rho})^T \mathcal{R} \mathbf{u}^\ell(\boldsymbol{\rho}) \right|^2, \quad (\text{S25})$$

under the constraint that  $\boldsymbol{\rho}$  is a unit norm vector (since the SLM can only redistribute the laser energy but it cannot regenerate energy), then classical results in linear algebra imply it is maximized by the largest eigenvector of  $\mathcal{R}$ . Moreover, up to known constants, the gradient derived in Eq. (S22) is basically a multiplication of the previous guess by the reflection matrix. However, as demonstrated in Fig. 4 of the main paper, given a coherent target averaging over an area is crucial for getting a good wavefront correction. If one attempts to optimize the confocal intensity at a single point, interference can bring all light into a strong point at the sensor, without actually focusing the light into a single point inside the volume. Attempting to adjust power algorithms to produce different modulations may require ad-hoc additions. However defining a target score and deriving its gradient provides a more principle framework to impose desired properties on the modulation.

In particular [2] used a variant of power iterations with incoherent fluorescent sources. The convergence of this incoherent version was a bit hard to analyze, and to justify it the supplementary file of [2] uses a model assuming the phase of the wavefront is captured precisely with a point diffraction interferometer. Their incoherent phase estimation is equivalent to the point-diffraction interferometry setup derived above.

#### 5. ADDITIONAL RESULTS

**Confocal scan captured images:** In Fig. S5 we display a super-position of images captured by the main and validation cameras. We average in one frame a sparse subset of the target points  $\ell$  in the area we scanned. We show the results before and after optimization for the result presented on the second row of Fig. 5 of the main text. Before optimization, the wavefront reaching the main camera is significantly aberrated. After optimization, clear focal points reflected from the chrome are observed. In the validation camera, we observe the wavefront reaching the target plane. Without modulation, the wavefront is highly aberrated, whereas after optimization, a well-defined focus is visible on the target plane. Areas covered by chrome are not observable in the validation camera because the chrome attenuates light. For visualization purposes, all images were normalized by their maximum value. However, in reality, without modulation, the light reaching both cameras is spread across the sensor, and these images would appear dark if normalized by the maximum value with modulation.

The resolution target in the in Fig. 5 in the main paper is constructed from four scanned iso-planatic patches. In Fig. S6 we show the different confocal scan from the different iso-planatic patches and their corresponding phase-masks

**Onion cells:** To better visualize the onion cell target we image in Fig. 7 of the main paper, we present a larger view through the validation camera Fig. S7 To validate our result of scanning onion cells through scattering medium, we also show a scan of a thin layer of onion cells, so light passes though osmosis without much scattering Fig. S8. We see that a reflective confocal image of onion cells without scattering is similar to what we have achieved in Fig. 7 of the main papers, where the cells themselves are reflecting light and the gap between them appears darker. In Fig. S9 we show the results from different iso-planatic patches. The final result presnted in the main paper in Fig.7 is composed from the iso-planatic patches, stitched two form the large field-of-view image. The patches partially overlap and to find the overlap between patches we used template matching. The image in Fig.7 in the paper was rotated for convenience of view.

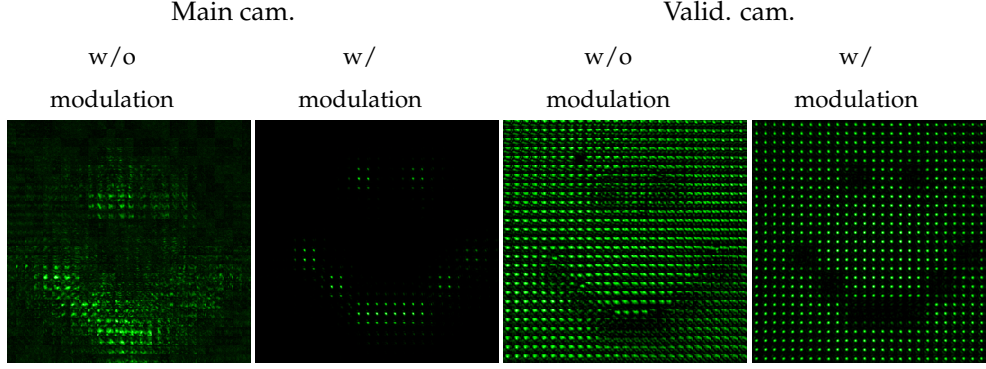


**Fig. S5. Focus after optimization:** We present the scanning results before and after optimization for both imaging (Main camera) and the target plane (Validation camera). Before optimization the light is scattered over the target plane and at the imaging plane. After optimization, we get good focus on both main and validation camera. Areas with coated chrome reflect more light resulting in brighter spots on the main camera. The chrome significantly attenuates the forward scattered light, hence they appear as black spots in the validation camera. All images were normalized to the maximum value of the image for visualization purposes.

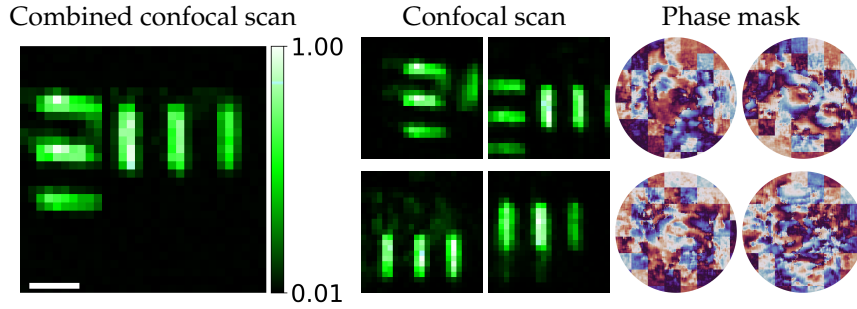


**Fig. S6. Iso-planatic patches of resolution target:** We show the iso-planatic patches that compose the combined result of the resolution target presented in Fig. 5 in the main paper. The first column shows the result presented in the main paper. The second and third columns show the iso-planatic patches which were scanned by our algorithm. The fourth and fifth columns shows the phase mask used for each iso-planatic patch. The iso-planatic patches were combined using a template matching algorithm.

## REFERENCES

1. D. Aizik and A. Levin, "Non-invasive and noise-robust light focusing using confocal wavefront shaping," *Nat. communications* **15** (2024).
2. D. Aizik, I. Gkioulekas, and A. Levin, "Fluorescent wavefront shaping using incoherent iterative phase conjugation," *Optica* **9**, 746–754 (2022).
3. L. M. Mugnier, A. Blanc, and J. Idier, "Phase diversity: A technique for wave-front sensing and for diffraction-limited imaging," (Elsevier, 2006), pp. 1–76.
4. L. Armijo, "Minimization of functions having Lipschitz continuous first partial derivatives." *Pac. J. Math.* **16**, 1 – 3 (1966).
5. P. Balondrade, V. Barolle, N. Guigui, *et al.*, "Multi-spectral reflection matrix for ultrafast 3d label-free microscopy," *Nat. Photonics* **18**, 1097–1104 (2024).
6. Y. Zhang, M. Dinh, Z. Wang, *et al.*, "Deep imaging inside scattering media through virtual spatiotemporal wavefront shaping," *arXiv preprint arXiv:2306.08793* (2024).
7. Y. Lee, D. Kim, Y. Jo, *et al.*, "Exploiting volumetric wave correlation for enhanced depth imaging in scattering medium," *Nat. communications* **14** (2023).
8. S. Kang, Y. Kwon, H. Lee, *et al.*, "Tracing multiple scattering trajectories for deep optical



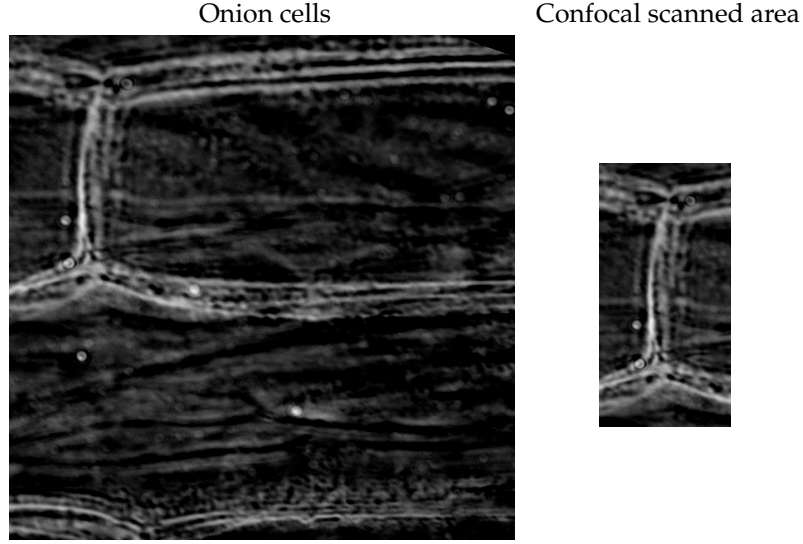


**Fig. S7. Onion cells:** We show a larger view captured by our validation camera of the onion cells example from Fig. 7 of the main paper

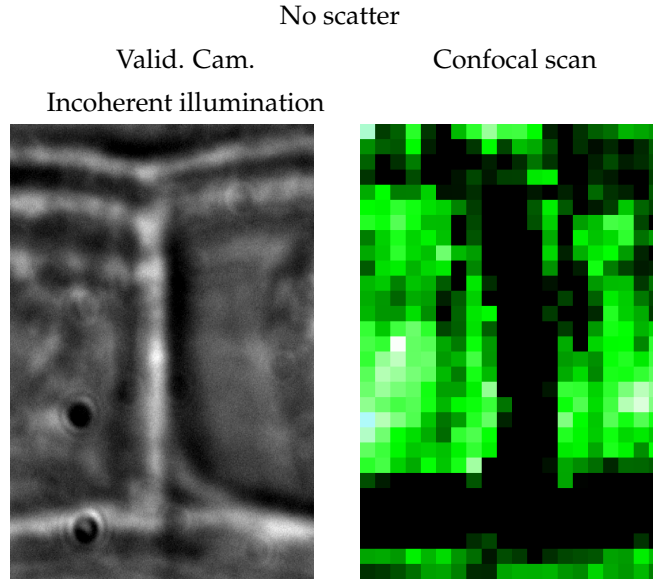


**Fig. S8. Onion cells without scattering:** We present a confocal scan of onion cells without scattering material. The onion cells here are different than the ones presented in the main text; however, we are able to see similar image.

- imaging in scattering media," *Nat. communications* **14** (2023).
9. O. Katz, E. Small, Y. Guan, and Y. Silberberg, "Noninvasive nonlinear focusing and imaging through strongly scattering turbid layers," *Optica* **1**, 170–174 (2014).
10. G. Osnabrugge, R. Horstmeyer, I. N. Papadopoulos, *et al.*, "Generalized optical memory effect," *Optica* **4**, 886–892 (2017).
11. M. Alterman, C. Bar, I. Gkioulekas, and A. Levin, "Imaging with local speckle intensity correlations: theory and practice," *ACM TOG* (2021).
12. B. H. Dean and C. W. Bowers, "Diversity selection for phase-diverse phase retrieval," *J. Opt.*

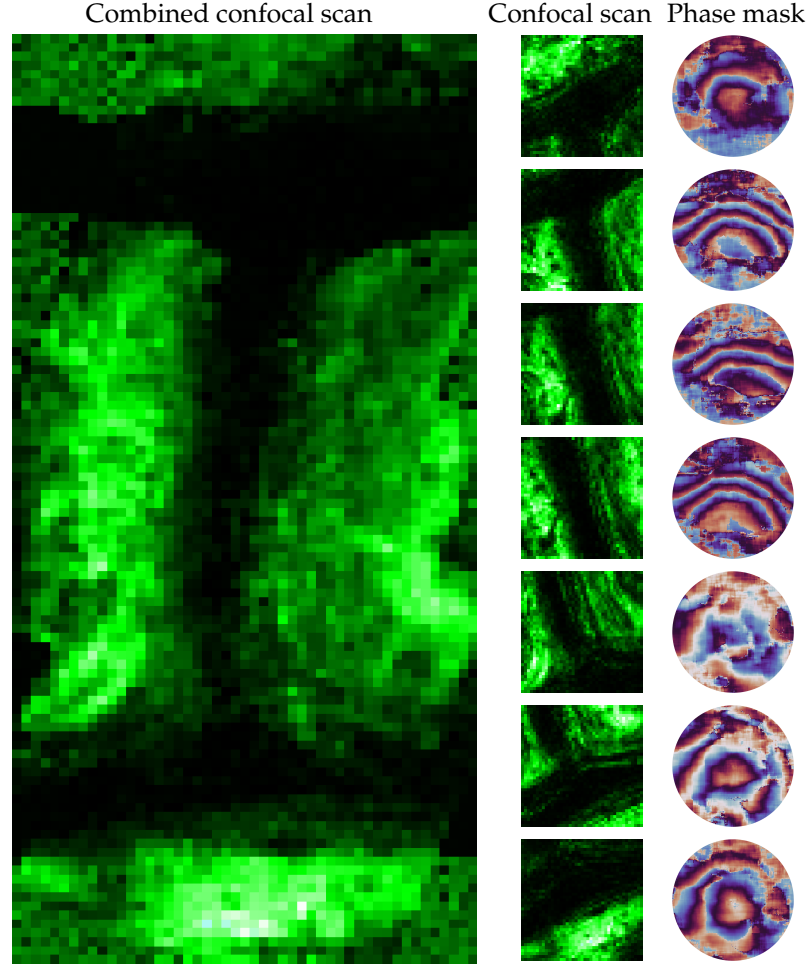


**Fig. S9. Iso-planatic patches in onion result:** We show the iso-planatic patches that compose the combined result of the onion cells boundary presented in Fig. 7 in the main paper. The first column shows the result presented in the main paper. The second column shows the iso-planatic patches which were scanned by our algorithm. The third column shows the phase mask used for each iso-planatic patch. The iso-planatic patches were combined using a template matching algorithm.

- Soc. Am. A **20**, 1490–1504 (2003).
13. R. A. Gonsalves, "Phase Retrieval And Diversity In Adaptive Optics," Opt. Eng. **21**, 215829 (1982).
  14. E. J. Candes, X. Li, and M. Soltanolkotabi, "Phase retrieval via wirtinger flow: Theory and algorithms," IEEE Transactions on Inf. Theory **61**, 1985–2007 (2015).
  15. R. N. Smartt and W. H. Steel, "Theory and application of point-diffraction interferometers," Jpn. J. Appl. Phys. **14**, 351 (1975).
  16. V. Akondi, A. Jewel, and B. Vohnsen, "Digital phase-shifting point diffraction interferometer," Opt. Lett. **39**, 1641–4 (2014).
  17. H. C. Song, W. A. Kuperman, W. S. Hodgkiss, *et al.*, "Iterative time reversal in the ocean," The J. Acoust. Soc. Am. **105**, 3176–3184 (1999).
  18. C. Prada, J.-L. Thomas, and M. Fink, "The iterative time reversal process: Analysis of the convergence," The J. Acoust. Soc. Am. **97**, 62–71 (1995).
  19. H. Ruan, M. Jang, B. Judkewitz, and C. Yang, "Iterative time-reversed ultrasonically encoded light focusing in backscattering mode," Sci. reports **4**, 7156 (2014).
  20. K. Si, R. Fiolka, and M. Cui, "Breaking the spatial resolution barrier via iterative sound-light



- interaction in deep tissue microscopy," *Sci. reports* **2**, 748 (2012).
21. I. Papadopoulos, J.-S. Jouhannau, J. Poulet, and B. Judkewitz, "Scattering compensation by focus scanning holographic aberration probing (f-sharp)," *Nat. Photonics* (2016).
  22. S. Kang, P. Kang, S. Jeong, *et al.*, "High-resolution adaptive optical imaging within thick scattering media using closed-loop accumulation of single scattering," *Nat. Commun.* **8**, 2157 (2017).
  23. U. Najar, V. Barolle, P. Balondrade, *et al.*, "Harnessing forward multiple scattering for optical imaging deep inside an opaque medium," *Nat. Commun.* **15**, 7349 (2024).